

1 **Raman Spectroscopy Study of Manganese Oxides – Layer Structures** **Revision 1**

2

3 Jeffrey E. Post¹, David McKeown², Peter J. Heaney³

4

5 *¹Department of Mineral Sciences, National Museum of Natural History, Smithsonian Institution,*

6 *Washington, DC, 20013-7012, USA; ²Vitreous State Laboratory, The Catholic University of*

7 *America, Washington, DC 20064, USA; ³Department of Geosciences, Penn State University, 540*

8 *Deike Building, University Park, PA 16802, USA*

9

10 *Corresponding author: Jeffrey Post, postj@si.edu

11

12

13

14 **Abstract**

15 Raman spectra were collected for an extensive set of well-characterized layer-structure
16 Mn oxide mineral species (phylломanganates) employing a range of data collection conditions.
17 We show that the application of a variety of laser wavelengths, such as 785, 633, and 532 nm, at
18 low power levels (30 – 500 μW) in conjunction with the comprehensive database of standard
19 spectra presented here, makes it possible to distinguish and identify the various phylломanganate
20 minerals. The Raman mode relative intensities can vary significantly as a function of crystal
21 orientation relative to the incident laser light polarization direction as well as incident laser light
22 wavelength. Consequently, phase identification success is enhanced when using a standards
23 database that includes multiple spectra collected for different crystal orientations and with
24 different laser light wavelengths. The position of the highest frequency Raman mode near 630-
25 665 cm^{-1} shows a strong linear correlation with the fraction of Mn^{3+} in the octahedral Mn sites.
26 With the comprehensive Raman database of well-characterized Mn oxide standards provided
27 here (and available online as supplemental materials), and use of appropriate data collection
28 conditions, micro-Raman is a powerful tool for identification and characterization of biotic and
29 abiotic Mn oxide phases from diverse natural settings, including on other planets, as well as for
30 laboratory and industrial materials.

31

32 Keywords: Manganese Oxide, Raman Spectroscopy, Phylломanganates, Birnessite

33

34

35

36

INTRODUCTION

37 Layer-structure Mn oxide minerals, also called phyllomanganates, are found in a wide
38 variety of geological settings and are important constituents in many soils and sediments (Post,
39 1999). These phases can precipitate from solution as the result of macro or microscale changes
40 in redox conditions, pH, or composition; additionally, natural and laboratory Mn oxides that
41 form by biologically mediated processes are predominantly phyllomanganates (McKeown and
42 Post 2001; Tebo et al. 2004; Santelli et al. 2011). Phyllomanganates having a birnessite-like
43 structure readily participate in redox and cation-exchange reactions and exhibit high adsorption
44 capacities for a variety of organic pollutants and toxic metallic ions (Le Goff et al. 1996;
45 Manning et al. 2002; Feng et al. 2007; Lopano et al. 2009; Kwon et al. 2013; Fleegeer et al. 2013;
46 Shumlas et al., 2016; Kong et al. 2019). They also have been identified as promising
47 heterogeneous compounds for water-oxidation catalysis (Sauer and Yachandra, 2002; Jiao and
48 Frei, 2010; Wiechen et al., 2012; Frey et al.; 2014; Feng et al., 2017). Phyllomanganates are
49 critical battery materials and are being investigated for their applications as catalysts and cation-
50 exchange agents, as well as for their potential to mitigate hazardous materials in the environment
51 (Ghodbane et al. 2009; Li et al. 2012; Nam et al. 2015).

52 Phyllomanganates are constructed of sheets of MnO_6 octahedra. The Mn is
53 predominantly Mn^{4+} but can be substituted by Mn^{3+} and vacancies, with the resulting layer
54 charges being compensated by various interlayer cations in the different phases (Fig. 1). Most
55 phyllomanganates also have interlayer water molecules. Natural samples commonly are fine-
56 grained and poorly crystalline, and the particular phyllomanganate mineral phases are difficult to
57 distinguish visually in the field or in hand specimens. They also can occur as fine-scale
58 intergrowths of two or more phases that readily alter from one to another. In many cases, X-ray

59 diffraction (XRD) of these phases also fails to identify them, since the XRD patterns often
60 exhibit broad peaks from multiple disordered phases, making basic phase identification difficult
61 or impossible (Ling et al. 2020). Consequently, many researchers employ other methods in
62 addition to XRD to characterize natural phyllomanganates, such as X-ray absorption
63 spectroscopy (XAS), Fourier transform infrared spectroscopy (FTIR), transmission electron
64 microscopy (TEM), and combined energy-dispersive X-ray spectroscopy and scanning electron
65 microscopy (EDS-SEM). These techniques also have experimental limitations and requirements,
66 such as special sample preparation methods, large sample sizes, or synchrotron X-ray sources.

67 Due to the difficulties of working with complex and typically poorly crystalline natural
68 phyllomanganate samples, many researchers use synthetic phases that are presumed to be
69 suitable analogs of the minerals. Offsetting the advantages of working with pure, relatively well-
70 crystalline laboratory-produced samples is the difficulty of assessing their relevancy to natural
71 phases or systems. Additionally, complexities and confusion introduced using multiple synthesis
72 methods, and terminology, can cause problems comparing results among different research
73 groups.

74 In a recent paper, we demonstrated the advantages of using micro-Raman spectroscopy to
75 routinely identify and characterize tunnel-structure Mn oxide phases for a variety of natural and
76 synthetic samples (Post et al. 2020). Here we extend that work to the phyllomanganates. During
77 the past few decades, numerous reports have described applications of Raman spectroscopy to
78 Mn oxides, primarily as an identification tool, but also for investigating changes in response to
79 certain redox, cation-exchange, and other reactions (Bernard et al. 1993). There are several
80 studies that have used Raman spectroscopy to study phyllomanganates (e.g. Bernard et al. 1993;
81 Kim and Stair 2004; Julien et al. 2003; Julien et al. 2004; Hsu et al. 2011; Burlet and Vanbrabant

2015; Yang et al. 2019; Boumaiza et al. 2019; and Bernardini et al. 2019) with various degrees of success. Such work has been invigorated in part by advancements in micro-Raman techniques that have resulted in greater availability of in-house Raman systems. Modern systems typically offer multiple laser options with high-sensitivity detectors that provide a range of data collection conditions that can be optimized for particular samples. Additionally, Raman spectrometers fitted with high quality microscopes permit rapid *in situ* interrogation of samples with spatial resolution approaching one micron or less. Micro-Raman systems have the potential to provide phase identification and structural information quickly and easily from discrete areas on natural or synthetic Mn oxide samples. In particular, the combination of Raman microscopy and analytical SEM provides unparalleled insights into the micro-mineralogy and -chemistry of complex samples.

Our study of the tunnel structure Mn oxides (Post et al. 2020) confirmed the importance of using low laser powers (e.g. < 0.35 mW) and multiple laser wavelengths (e.g. 532, 633, and 785 nm) in order to obtain the most useful Raman spectra for phase identification and for elucidating structure information. These considerations are critical for the large tunnel-structure Mn oxides, such as todorokite and romanechite, but are equally so for the phyllosulfates, and in particular, for the birnessite-like phases that are important in many natural systems.

In the work presented here, we provide results from the most comprehensive-to-date Raman spectroscopy study of layer-structure Mn oxide phases. Raman spectra were collected from a large number and variety of natural and synthetic samples, drawing from the Smithsonian Institution mineral collection, and additional samples from various sources, which had been characterized in detail as part of our long-term research program on Mn oxides. Raman spectra were collected using multiple Raman systems with a range of laser wavelengths in order to

105 provide comparisons and to determine optimal data collection conditions. Additionally, we
106 present representative spectra from different specimens, localities, and crystal orientations. A
107 major goal of this study is to provide a spectral database for identifying the various layer-
108 structure Mn oxide mineral phases, with an emphasis on natural samples. Finally, we explore
109 spectral trends and details for some specific phases that provide insights about composition,
110 symmetry, and in some circumstances, Mn oxidation states.

111

112 **EXPERIMENTAL METHODS**

113 **Specimens**

114 The layer-structure Mn oxide mineral samples for which spectra are presented here are
115 listed in Table 1, including information about individual compositions. Structure symmetry and
116 factor group analyses (Fateley et al. 1972) for the various phases are presented in Table 2. A
117 variety of samples were included to represent variations in composition, structural disorder, and
118 locality. All samples were checked by powder X-ray diffraction (XRD) to confirm phase
119 identification and purity. Energy-dispersive X-ray spectroscopy (EDS) analyses and
120 backscattered electron imaging were used to determine composition and assess chemical
121 homogeneity. Where possible, single crystals, or crystal fragments, were selected for Raman
122 measurements; fine-grained samples were lightly crushed, or in some cases, prepared as polished
123 sections that were also used for chemical analyses. For some Raman measurements, loose
124 sample grains were placed on glass slides without adhesive, which can introduce strong
125 luminescence. The synthetic triclinic Na-birnessites included the same material studied by Post
126 and Veblen (1990) as well as samples more recently synthesized and described in Ling et al.
127 (2018). Synthetic birnessites with different compositions were prepared by cation-exchange,

128 following the procedure of Golden et al. (1986). The hexagonal birnessite samples were
129 prepared by reacting Na-birnessite with a pH 2 HCl solution.

130 **X-ray diffraction (XRD)**

131 Samples were characterized by powder XRD using a Rigaku II D/MAX-RAPID micro-
132 diffractometer (Department of Mineral Sciences, Smithsonian Institution) equipped with a
133 graphite monochromator and a curved image plate area detector. A Mo tube (50 kV, 40 mA) was
134 used as the X-ray source with a 0.3 mm collimator. Small (~1 mm) balls of powdered samples
135 (with added super-glue as needed), or fragments of fine-grained polycrystalline materials, were
136 mounted on tips of glass fibers. During exposure to X-rays, the sample was rotated at 1°/min on
137 phi to minimize the effects of sample heterogeneity and preferred orientation. The full set of
138 Debye-Scherrer diffraction rings from the imaging plate data were integrated using Rigaku-
139 provided software, and interpretation of XRD patterns was performed using the JADE 9 software
140 package. Phase identifications were confirmed using the ICDD PDF-4 Minerals database and an
141 in-house collection of well-characterized Mn oxide mineral standards. Representative XRD
142 patterns are deposited as supplementary data with *American Mineralogist*.

143

144 **Scanning electron microscopy**

145 Uncoated samples (which then could also be used for Raman analysis) were mounted on
146 carbon tape adhered to an aluminum stub and analyzed with scanning electron microscopy
147 (SEM) using a field emission source (FEI Apreo) equipped with an EDAX Octane Silicon Drift
148 EDS detector (Department of Mineral Sciences, Smithsonian Institution). Backscattered electron
149 (BSE) images were collected, and EDS analysis was used to determine the chemical composition
150 and homogeneity of the Mn oxide samples (with beam current of 1.6 nA). The images were

151 collected and analyses performed in low vacuum (0.31 torr) at an accelerating voltage of 15 kV.

152 The data were processed using the Noran System Six 3 (NSS 3) software.

153

154 **Raman spectroscopy**

155 The reproducibility of the Raman spectra and the optimal data collection conditions were
156 evaluated by using four different micro-Raman systems at 25 °C in back-scattering geometry
157 using a single-grating spectrograph with notch filters. Two HORIBA LabRam HR Evolution
158 systems were employed (Department of Mineral Sciences, Smithsonian Institution; and Materials
159 Characterization Laboratory, Penn State University), both equipped with Synapse back-
160 illuminated deep depleted, Peltier cooled 1024 x 128 element CCD cameras. The spectra
161 presented in this paper were collected using 532, 633 (Penn State), and 785 nm solid state lasers
162 with 300 and 600 gr/mm spectrograph gratings, respectively, for spectral resolutions near 4 cm⁻¹.
163 An Olympus 100x or 50x objective was used to focus the incident laser light onto the sample.
164 The characteristic 520 cm⁻¹ line from a Si wafer standard was used for Raman frequency
165 calibration. The laser power at the sample was measured using a Thorlabs power meter
166 (PM100USB) for the various combinations of microscope objectives and lasers. Typically,
167 spectra were collected using laser powers of 540 μW or less for the 532 nm laser and 350 μW or
168 less for the 633 and 785 nm lasers. Some phases, e.g. chalcophanite and lithiophorite, did not
169 exhibit obvious spectral changes at laser powers up to 2 mW, but birnessite-like phases showed
170 evidence of sample degradation or phase transformation at laser powers above ~500 μW at the
171 sample. For the 532 nm laser, spectra for birnessite-like phases exhibited changes at powers as
172 low as 30 μW. The laser power measurements are intensities of the focused incident laser beam

173 at the sample, not power densities, which vary depending upon the laser spot size, determined by
174 the objective used, laser focus, and certain other instrumental and sample surface characteristics.

175 The second system (Vitreous State Laboratory, Catholic University) consists of a WITec
176 alpha-300 RA+ micro-Raman system, where 633 nm solid state diode and 532 nm DPSS lasers
177 were used with a 600 gr/mm grating to disperse the Raman scattered light on to a 1024 x 128
178 element Peltier cooled CCD camera (Andor Technology Model DV401A-BVF-352). 50x and
179 100x Zeiss objectives were used producing a $\sim 1 \mu\text{m}$ laser spot size on the sample. The spectra
180 were frequency calibrated to the Si 520 cm^{-1} mode. The spectral resolution of the data produced
181 from these system configurations is near 6 cm^{-1} . Spectra for birnessite-like phases showed phase
182 alteration at powers as low as $150 \mu\text{W}$ using 633 nm laser light.

183 A third system (Vitreous State Laboratory, Catholic University) consists of a Melles-Griot
184 Model 45 Ar⁺ laser that provided 457.9 and 514.5 nm wavelength light that was guided through a
185 long working distance Mitutoyo 10x microscope objective and focused to a $10 \mu\text{m}$ diameter spot
186 on the sample. The scattered light proceeded through holographic notch and super-notch filters
187 (Kaiser Optical Systems), which reduced the Rayleigh (or elastically) scattered light intensity by
188 ten optical densities. The Horiba HR460 spectrograph used a 1200 gr/mm grating (Richardson
189 Grating Laboratory) to disperse the Stokes scattered light from the sample on to a 2048 x 512
190 element Peltier cooled CCD detector (Andor Technology Model DU440BV). Due to the
191 relatively broad spectral features for most samples measured, the spectrograph incident slits were
192 set to 6 cm^{-1} spectral resolution. The spectrograph was frequency calibrated using CCl_4 ,
193 such that recorded Raman mode frequencies for all spectra are accurate to within $\pm 1 \text{ cm}^{-1}$ of the
194 actual values. The laser power for this system was minimized to $< 0.1 \text{ mW}$ at the sample to avoid
195 sample heating and alteration.

196 For each sample, initial data collection was performed using minimal laser power, e.g. 30
197 μW ; the power level was gradually increased until noticeable changes occurred to the spectra,
198 such as variations in peak intensities, the appearance of new peaks, or broad band luminescence
199 with evidence of sample darkening or hole formation at the incident laser light position. Where
200 possible, relatively flat and smooth sample surfaces, as ascertained at 100x or 50x magnification,
201 were selected for data collection, using 5- to 60-second integration times per acquisition, with
202 two to 10 acquisitions per spot to improve signal-to-noise levels in the spectra. Crystal
203 orientation effects were apparent for most layer-structure Mn oxide phases. Phylломanganate
204 crystals typically have a platy morphology and tended to orient preferentially with the Mn
205 octahedral sheets normal to the direction of the laser beam. When possible, spectra were
206 collected with crystals oriented such that the octahedral sheets were both parallel and
207 perpendicular to the direction of the incident laser light. Polarized spectra were gathered using
208 an analyzer polarizer inserted in the scattered light path. Polarized spectra were labeled VV
209 (vertical-vertical) or VH (vertical-horizontal) to describe collection conditions where the laser
210 light polarization was oriented parallel or perpendicular, respectively, to the polarization
211 direction of the analyzer. For comparison, unpolarized spectra also were collected without an
212 analyzer in the scattered light path between the sample and spectrograph.

213

214 **Lattice Dynamics Calculations**

215 In order to provide guidance for some general vibrational assignments to the observed
216 Raman features, preliminary normal coordinate valence-force lattice dynamics (LD) calculations
217 at zero wavevector (Dowty 1987 and 2007) were performed for several of the phylломanganate
218 structures. The models included Mn-O stretch as well as O-Mn-O bend force constants to

219 simulate the various bonding environments within the linked MnO_6 octahedra. Interlayer cation-
220 oxygen stretch force constants were also included. The force constants were allowed to vary so
221 that the calculated mode frequencies best matched the set of observed mode frequencies from the
222 Raman spectra for each phase.

223 Overall, LD calculations indicated that Raman-active modes for these Mn-oxides can be
224 divided into two frequency ranges. Consistent with previous interpretations by Julien et al.
225 (2003, 2004), modes above 500 cm^{-1} , are dominated by MnO_6 octahedral deformations,
226 including O-Mn-O bend, Mn-O stretch, as well as expansion and compression of the octahedra in
227 the layer stacking direction, and shear motions of layers of O atoms that are parallel to the MnO_6
228 layers. In structures with higher symmetry Mn-sites, e.g. Mn on a symmetry center, the internal
229 Mn octahedral modes involve O motions, while the Mn atoms are stationary. Modes at
230 frequencies less than 500 cm^{-1} include contributions from displacements of interlayer cations,
231 such as Zn^{2+} in chalcophanite and Na^+ in birnessite, and cation-water and water-water
232 interactions.

233

234

235

RESULTS

236 Chalcophanite Group

237 Chalcophanite ($\text{ZnMn}_3\text{O}_7 \cdot 3\text{H}_2\text{O}$; Space Group *R*-3) is constructed of sheets of Mn^{4+} -O
238 octahedra with one out of seven octahedra vacant. Single-crystal X-ray diffraction studies (Post
239 and Appleman 1988) indicate that the vacancies are fully ordered within the octahedral sheets.
240 Zn^{2+} cations sit above and below the vacancies and are in octahedral coordination with three O
241 atoms from the octahedral sheet and three O atoms from the interlayer water molecules (Fig. 1).
242 Jianshuiite and ernienickelite are isostructural with chalcophanite, but have Mg^{2+} and Ni^{2+} ,

243 respectively, as the dominant interlayer cations. Chalcophanite group minerals commonly occur
244 as euhedral platy crystals.

245 Chalcophanite typically gives strong Raman features, especially for 532 and 633 nm laser
246 light that are consistent for laser powers less than ~ 0.5 mW. Chalcophanite spectra are highly
247 sensitive to laser light polarization, especially the Mn-O vibrational modes near 670 cm^{-1} that are
248 intense in parallel polarized light but almost absent in the crossed polarized spectrum (Fig. 2).
249 Similar polarization behavior for these modes is also observed for other phyllophanates. By
250 contrast, there are only small intensity differences for analogous peaks in crossed versus parallel
251 polarized spectra for the large tunnel structure phases such as todorokite and romanechite (Post
252 et al. 2020). Raman spectra for chalcophanite using 532, 633 and 785 nm lasers are similar (Fig.
253 3). The 670 cm^{-1} mode for chalcophanite has the greatest frequency of any of the layer Mn
254 oxides, presumably because all the Mn is in the 4+ valence state, which imposes the shortest
255 possible average Mn-O distance, and correspondingly the highest frequency vibrational motions.
256 As discussed below, substitution of Mn^{4+} by the larger Mn^{3+} , with its attendant Jahn-Teller
257 distortions, shifts the corresponding peaks to lower frequencies and increases the number of
258 internal MnO_6 modes.

259 The Raman spectra for chalcophanite, jianshuiite, and ernienickelite are similar, but
260 some variations, e.g. extra peaks near 533 and 590 cm^{-1} , suggest some fundamental differences
261 in the Ni-bearing ernienickelite (Fig. 4). A detailed structure refinement has not been reported
262 for ernienickelite. Spectra collected from chalcophanite with the laser light polarization
263 direction parallel versus perpendicular to the octahedral sheets (Fig. 5a) show modest variations
264 in intensities of several modes. Spectra collected with the laser polarization perpendicular to the
265 layers for chalcophanite and ernienickelite show modes at ~ 3320 and 3390 cm^{-1} (Fig. 5b) that

266 correspond to OH stretch vibrations from the interlayer water molecules; these modes were
267 absent in spectra collected with the laser polarization parallel to the octahedral sheets, indicating
268 that the predominant OH stretch motion is perpendicular to the sheets.

269 Lattice dynamic calculations for the chalcophanite structure (Figs. 6a and b) indicate that
270 modes above $\sim 500 \text{ cm}^{-1}$ are due primarily to internal MnO_6 deformation, as well as expansion
271 and compression of the MnO_6 layers. There are also Zn-O stretch contributions with Zn
272 translating perpendicular to the octahedral layers, but as there are more MnO_6 octahedra than
273 ZnO_6 octahedra, these modes are dominated by internal MnO_6 displacements. Modes below 500
274 cm^{-1} arise from mixtures of MnO_6 deformations and motions involving the interlayer Zn^{2+}
275 cations and water molecules in ZnO_6 octahedra, where three of the coordinating oxygens are
276 from water molecules. The Zn-H₂O stretch and the water motions become more dominant in the
277 lower frequency modes. The lower frequency parallel polarized A_g modes arise from Zn
278 translations perpendicular to the octahedral layers, while lower frequency crossed polarized B_g
279 modes result primarily from Zn translations parallel to the octahedral layers. Not surprisingly,
280 the most obvious differences among the spectra for chalcophanite compared with those for
281 jianshuiite and ernienickelite are in this lower frequency region, presumably related to the
282 different sizes and bonding properties of the Zn^{2+} versus Mg^{2+} and Ni^{2+} interlayer cations,
283 respectively.

284

285 **Ranciéite Group**

286 Ranciéite, a Ca-rich phyllomanganate, has been found as an abiotic product in low-
287 temperature alpine vein deposits and in oxidized zones of Fe and Mn deposits (Ertle et al. 2005).
288 Recent studies, however, of naturally occurring phyllomanganates from fresh-water

289 environments revealed Ca to be the predominant interlayer cation, sometimes associated with
290 Mg, Ba, and/or K (Bargar et al. 2009; Tan et al. 2010; Ling et al. 2020). Furthermore, ranciéite-
291 like structures play critical roles in water-oxidation catalysis and as the oxygen-evolving
292 complex within the enzyme photosystem II (PSII) (Umena et al. 2011; Zhang et al. 2015;
293 Yamaguchi et al. 2017).

294 Ranciéite has a hexagonal structure (*P*-3), and like chalcophanite consists of sheets of
295 Mn^{4+}O_6 octahedra, but with one out of ten (or eleven) octahedra vacant, and Ca^{2+} and water
296 molecules in the interlayer regions (Kim 1991, Post et al. 2008). X-ray diffraction and selected
297 area electron diffraction patterns show no superstructure reflections, indicating that vacancies are
298 not ordered in the octahedral sheets, presumably because of the relatively fewer vacancies, and
299 therefore less energetic drive to order, compared with chalcophanite. The interlayer cations
300 occupy sites above and below the octahedral vacancies and are predominately Ca^{2+} in ranciéite
301 and Mn^{2+} in takanelite; other similar sized divalent cations, such as Ba^{2+} , Sr^{2+} , and Mg^{2+} are
302 commonly found in ranciéite and takanelite specimens (Table 1 and Kim 1991). The interlayer
303 cations are coordinated to three octahedral O atoms and three interlayer water O atoms. The
304 interlayer-cation to Mn octahedral site ratio is ~ 0.2 (compared to 0.33 in chalcophanite), and the
305 total interlayer cation charge is approximately +0.75. The larger sizes of the interlayer cations in
306 ranciéite relative to those in chalcophanite group minerals might limit the numbers of cations that
307 can fit into the interlayer region. The chemical analyses for the ranciéite samples used in this
308 study, as well as Mn and interlayer cation occupancy factors determined by Rietveld refinements
309 (Post et al. 2008), indicate that Mn^{2+} is absent or present in only minor amounts as an interlayer
310 cation. The powder X-ray diffraction patterns and Raman spectra suggest that the ranciéite

311 structure is like those of the synthetic Ca-birnessites generated when Na-birnessite is exchanged
312 at low pH and low Ca concentrations (Elmi et al. 2020).

313 As with chalcophanite, the parallel and crossed polarized spectra of ranciéite (Fig. 7)
314 reveal a strong polarization response, especially for the A_g internal MnO_6 modes near 667 and
315 578 cm^{-1} , which arise from mostly symmetric stretch vibrations that can only effectively scatter
316 light polarized in the same direction as the incident laser beam; hence, these prominent high
317 frequency features nearly disappear in the cross polarized spectrum. Unpolarized ranciéite
318 spectra collected using 532, 633 and 785 nm laser wavelengths are plotted in Figure 8, and for
319 several different ranciéite specimens in Figure 9. Not surprisingly, there is a resemblance
320 between the chalcophanite and ranciéite spectra, but the ranciéite peaks generally are broader,
321 presumably because of the lower crystal structure symmetry for ranciéite (P -3 vs. R -3), and the
322 disordered vacancies in the octahedral sheets. Also, modes below 300 cm^{-1} are weaker or absent
323 for ranciéite, relative to chalcophanite, likely resulting from interlayer cation disorder related to
324 the random Mn site vacancies, and the variety of interlayer cations commonly found in natural
325 samples. Powder XRD patterns for ranciéite samples typically exhibit broad diffraction peaks
326 that also suggest structural disorder. The highest frequency Raman modes observed for various
327 ranciéite specimens (near 667 cm^{-1}) are comparable to those seen in the chalcophanite spectra,
328 suggesting that the Mn is tetravalent; this is consistent with Rietveld refinements (Post et al.
329 2008) showing ranciéite Mn-O bond distances comparable to those reported for chalcophanite
330 (Post and Appleman 1988).

331 Ranciéite structure LD calculations (Fig. 10) include A_g modes at ~ 665 and 564 cm^{-1}
332 dominated by expansion - compression motions of the MnO_6 octahedral sheets parallel to the c -
333 axis, the layer stacking direction, with some Ca^{2+} translation parallel to the c -axis. Calculated E_g

334 modes at 621 and 396 cm^{-1} arise from MnO_6 octahedral shear within the layer. The lower
335 frequency modes are dominated by interlayer water translations parallel (443 and 508 cm^{-1}) or
336 perpendicular (363, 384, and 420 cm^{-1}) to the layer stacking direction. The calculations do not
337 explain the observed A_g mode near 605 cm^{-1} , nor most observed modes below 400 cm^{-1} (Fig. 8)
338 that may be due to motions of the interlayer cations (Ca^{2+}) near MnO_6 octahedra layer defects or
339 water molecules.

340

341 **Birnessite-like Phases**

342 Birnessite was first described by Jones and Milne (1956) as a natural phase discovered in
343 Aberdeenshire, Scotland with a chemical formula of $\text{Na}_{0.7}\text{Ca}_{0.3}\text{Mn}_7\text{O}_{14} \cdot 2.8\text{H}_2\text{O}$. Subsequently,
344 numerous natural phases with “birnessite-like” structures have been described, including
345 ranciéite (Post et al. 2008), takanelite (Nambu and Tanida 1971; Kim 1991), and lagalyite
346 (Witzke et al. 2017). They commonly occur as fine-grained, poorly crystalline aggregates and
347 coatings, making the studies of their structures and behaviors challenging. Additionally, various
348 synthetic birnessite-like structures containing almost every possible alkali and alkaline earth
349 element, as well as many of the transition metals, have been synthesized (*e.g.*, McKenzie, 1971;
350 Golden et al., 1986) in attempts to elucidate the structural and chemical features of birnessite-like
351 phyllomanganates (*e.g.*, Post and Veblen, 1990; Drits et al., 1997; Silvester et al., 1997; Lanson
352 et al., 2000; Post et al., 2002; Feng et al., 2004; Händel et al., 2013) and their reactivities (*e.g.*,
353 (Manceau et al., 2002; Feng et al., 2007; Lopano et al., 2007, 2011; Landrot et al., 2012; Wang et
354 al., 2010; Kwon et al., 2013; Lefkowitz et al., 2013; Yin et al., 2013; Fischel et al., 2015; Hinkle
355 et al., 2016; Zhao et al., 2016; Fischer et al. 2018). Laboratory studies have also demonstrated
356 that formation of birnessite-like phases can be initiated, or enhanced, by certain microbes and

357 fungi (Tebo et al. 2004; Webb et al. 2005; Grangeon et al. 2010; Santelli et al. 2011), and it is
358 therefore likely that biologically mediated birnessite-like phyllomanganates are important in
359 natural systems.

360 The birnessite structure is constructed of stacked layers of nominally Mn^{4+}O_6 octahedra;
361 substitution of Mn^{3+} or other lower valence cations and vacancies for Mn results in a net negative
362 charge on the octahedral sheets (Fig. 1). The charge is offset by addition of large mono- or
363 divalent cations (e.g. Na^+ , Ba^{2+} , K^+ , Ca^{2+}) into the interlayer region, along with water molecules.
364 Birnessite-like phases with predominantly Mn^{4+} exhibit overall hexagonal (trigonal) or near-
365 hexagonal symmetry. As the proportion of Mn^{3+} increases, the associated Jahn-Teller distortions
366 lower the symmetry to triclinic (Silvester et al. 1997; Ling et al. 2018). Birnessite-like structures
367 exhibit a characteristic ~ 7 Å repeat in the layer stacking direction. In buserite phases, a double
368 layer of water molecules between the octahedral sheets expands the layer spacing to ~ 10 Å.

369 Raman spectra collected using a 785 nm laser are shown for triclinic synthetic Na-
370 birnessite and hexagonal-birnessite in Figure 11. The octahedral layers in Na-birnessite
371 $[(\text{Na}^{+}_{0.29}, \text{Mn}^{2+}_{0.02}, \text{H}^{+}_{0.05}) (\text{Mn}^{3+}_{0.38}, \text{Mn}^{4+}_{0.62}) \text{O}_2 \cdot 0.75\text{H}_2\text{O}]$ (Post et al. 2002) have $\sim 38\%$ Mn^{3+}
372 (Ilton et al 2016) and no vacancies. H-birnessite has $\sim 20\%$ Mn^{3+} (Ilton et al 2016), mostly in the
373 interlayer region, and $\sim 10\%$ of the Mn octahedra are vacant (Ling et al 2018). The Raman
374 spectra collected for Na-birnessite using 457.9, 633 and 785 nm lasers are plotted in Figure 12a.
375 All spectra for birnessite-like phases collected using 532 nm laser light, even with power levels
376 at 0.03 mW, show significant evidence of alteration due to laser heating, presumably related to
377 the higher energy of the shorter wavelength light. Other observations suggest that 785 nm laser
378 light consistently yields reproduceable spectra with no evidence of sample degradation for laser
379 powers below about 0.3 mW. Spectra collected with 457.9 and 633 nm laser light at power

380 levels near 0.1 mW are similar to those for 785 nm (Fig. 12a), with indications of sample
381 alteration at powers as low as 0.15 mW (Fig. 12b).

382 LD calculations for Na-birnessite used a simplified higher symmetry $C2/m$ monoclinic
383 structure (the triclinic structure is close to having monoclinic symmetry), due to uncertainties
384 arising from disorder among the H, Na, and O(w) positions. Similar to other phyllomanganates,
385 LD calculations (Fig. 13) indicate that the highest frequency Raman peaks, e.g. the A_g mode at
386 640 cm^{-1} for Na-birnessite, arise primarily from MnO_6 octahedral expansion and compression
387 motions parallel to the layer stacking direction. The next highest frequency modes, A_g and B_g at
388 ~ 586 and 566 cm^{-1} , respectively, arise from shear motions of O atoms parallel to the MnO_6
389 layers. At frequencies below 500 cm^{-1} , calculated modes are dominated by translations of the
390 interlayer Na and H_2O .

391 Raman spectra collected from synthetic birnessite-like phases having different interlayer
392 cations are plotted in Figure 14. The spectra are similar at frequencies above 300 cm^{-1} , indicating
393 that the MnO_6 octahedral sheets were not generally affected by the exchanges of the interlayer
394 cations. A notable exception, however, involves the positions of the highest frequency peaks,
395 ranging from 651 cm^{-1} for Ca-birnessite to 636 cm^{-1} for K-birnessite. As described below, these
396 disparities likely reflect variations in Mn^{3+} concentration, which in turn depends on the valence
397 charges and sizes of the interlayer cations. The most noticeable differences among the various
398 birnessite spectra are in the lower frequency modes, which are governed by interlayer cation
399 motions, as shown by our LD calculations. These modes are most intense for triclinic structures
400 whose interlayer cations occupy positions at or near the midpoint between the MnO_6 layers, e.g.
401 for Na^+ , K^+ , Li^+ , and Ba^{2+} -birnessites (Post and Veblen 1990; Lopano et al. 2007). In some

402 cases, the Raman spectra might reveal the identity of the predominant interlayer cation and its
403 site symmetry; for example, a strong peak near 97 cm^{-1} is present only for K-birnessite (Fig. 14).
404 Also, compared with other compositions, K-exchanged birnessite typically showed sharper
405 Raman peaks, suggesting that K^+ is particularly well accommodated by the birnessite structure.

406

407 **Vernadite**

408 Vernadite is a poorly crystalline natural Mn oxide phase characterized by a powder XRD
409 pattern with broad peaks at 2.46, 1.42, and rarely at 2.2 Å. It was first described and named by
410 Betekhtin (1940). Vernadite is commonly described as a birnessite that is turbostratically
411 disordered in the layer stacking direction, or a birnessite with crystallites with so few MnO_6
412 layers that powder XRD patterns show no basal reflections (Buser et al. 1954; Bricker 1965;
413 Giovanoli, 1980; Drits et al. 1997; Grangeon, 2012). Chukrov et al. (1987) concluded, however,
414 that birnessite and vernadite are distinct. Chemical analyses of vernadite typically show minor
415 amounts of K, Mg, Ca, Ba, and Fe with 15-25 wt.% water as compared with approximately 12
416 wt.% water in Na-birnessite (Chukrov et al. 1978). Vernadite is found in the oxidized zone of
417 Mn-rich deposits and might be a major phase in ocean Mn nodules and crusts (Chukrov et al.
418 1987). Vernadite often is assumed to be analogous to the synthetic phase $\delta\text{-MnO}_2$ (Villalobos et
419 al. 2003; Grangeon, 2010; Lee et al. 2019), although the term $\delta\text{-MnO}_2$ has been applied very
420 broadly in recent years. Some have suggested that its formation is primarily mediated by biota
421 (Chukrov et al. 1987; Grangeon et al. 2012). Unpolarized and polarized Raman spectra for
422 vernadite from a Pacific Ocean crust (Table 1) contain a few broad peaks consistent with its
423 disordered nature (Fig. 15).

424

425 **Lithiophorite and Asbolane**

426 Lithiophorite is constructed of stacked sheets of MnO_6 octahedra alternating with sheets
427 of $\text{Al}(\text{OH})_6$ octahedra in which one-third of the octahedra are vacant (Fig. 1). In the idealized
428 structure, Li^+ cations fill the vacancies in the Al layer, and charge balance is maintained by Mn^{3+}
429 replacing one-third of the Mn^{4+} cations (Post and Appleman 1994). The layers are cross-linked
430 by H-bonds between the hydroxyl H^+ ions on the Al/Li layer and O atoms in the MnO_6 octahedra
431 sheet. Chemical analyses show that transition elements such as Ni, Co, and Cu commonly
432 substitute into the structure. Reported Li concentrations range from 0.2 to 3.3 weight % oxide
433 (Ostwald 1984). Lithiophorite typically occurs in oxidized zones of Mn deposits and in some
434 soils.

435 Polarized Raman spectra collected for lithiophorite (Fig. 16) show strong polarization
436 effects for the higher frequency peaks, similar to that observed for most other phyllosulfates.
437 The Raman spectra for lithiophorite from South Africa showed a curious for wavelengths of
438 514.5, 532, 633, and 785 nm laser light (Figs. 16 and 17), where Raman mode frequencies
439 increase by 10 to 30 cm^{-1} as laser wavelengths became shorter. One possible explanation for the
440 shift is that the shorter wavelength laser light oxidizes some of the Mn^{3+} to Mn^{4+} . We did not see
441 this effect for other lithiophorite, or phyllosulfate samples. The large broad band centered
442 near 340 cm^{-1} in the relatively weak 785 nm spectrum may be due to luminescence effects and
443 appears to overwhelm the Raman mode near 380 cm^{-1} seen in the shorter laser wavelength
444 spectra. This feature was especially prominent for the South African lithiophorite and less
445 obvious in 785 nm spectra for other lithiophorite samples. It is possible that the cause of the
446 luminescence is trace impurities unique to this sample. It also could be an orientation effect, as

447 this is the only sample that consisted of large plate-like crystals, which were oriented with their
448 flat surface perpendicular to the laser beam. Other lithiophorite samples typically were fine-
449 grained with random crystal orientations.

450

451 Because lithiophorite has alternating layers of $(\text{Mn}^{4+}, \text{Mn}^{3+}) \text{O}_6$ and $(\text{Al}, \text{Li})\text{O}_6$ octahedral
452 sheets, the structure contains a variety of octahedral environments: 1) Mn^{4+} in two-thirds of the
453 Mn octahedra, with average Mn-O distances of $\sim 1.89 \text{ \AA}$ (Post and Appleman 1994); 2) Jahn-
454 Teller distorted Mn^{3+} octahedra in one-third of the Mn sites, with average Mn-O distances of
455 $\sim 2.04 \text{ \AA}$ (Shannon 1976); and 3) two-thirds $\text{Al}(\text{OH})_6$ and one-third $\text{Li}(\text{OH})_6$ in the Al,Li
456 octahedral sheet, with Al-OH = 1.88 \AA and Li-OH = 2.10 \AA (Shannon 1976). This range of
457 octahedral environments likely contributes to the typically broader peaks in the spectra for
458 lithiophorite compared with those for chalcophanite. The lithiophorite spectra show no clear
459 features below 350 cm^{-1} , presumably because there are no interlayer cations or water molecules,
460 as there are in birnessite and chalcophanite phases.

461 LD calculations for lithiophorite (Fig. 18) indicate that A_{1g} modes above 500 cm^{-1} are
462 due to MnO_6 and $\text{Al}(\text{OH})_6$ octahedral sheet compression-expansion motions parallel to the c -
463 axis, whereas the higher frequency E_g modes are due to MnO_6 and $\text{Al}(\text{OH})_6$ octahedral sheet
464 shear motions perpendicular to the c -axis. Calculated modes below 500 cm^{-1} have major
465 contributions from O-H stretches parallel to the c -axis (A_{1g}) and H translations within the a - b
466 plane (E_g).

467 Asbolane is a lithiophorite-like phase with transition-metal cations such as Co, Cu and
468 Ni replacing some of the Al, and possibly Mn (Chukhrov et al. 1982; Manceau et al. 1987). The

469 asbolane structure has not been determined, but Chukhrov et al. (1982) propose that it likely has
470 hexagonal symmetry, and the lithiophorite $\text{Al}(\text{OH})_6$ layer is largely replaced by poorly structured
471 “islands” of $(\text{Co}, \text{Ni}, \text{Cu})\text{O}_6$ octahedra. Figure 19 shows that spectra for several asbolane
472 samples (Table 1) are similar to that of lithiophorite; a major difference is that the peak near 540-
473 560 cm^{-1} is relatively stronger for the asbolane spectra, increasing in intensity with greater Co
474 concentrations. Burlet and Vanbrabant (2015), based on results from a peak-fitting procedure,
475 suggested a correlation between certain peak positions and intensities and the compositions of
476 asbolane-lithiophorite samples; they also observed an intensity increase for a peak at $\sim 540 \text{ cm}^{-1}$
477 for asbolane relative to lithiophorite.

478

479 **Feitknechtite**

480 The crystal structure for feitknechtite is not known. The formula is assumed to be
481 MnOOH , and some have speculated that the structure consists of layered MnO_6 octahedra (Luo
482 et al. 1996, Grangeon et al. 2017). Our XPS data (unpublished results) confirm that all Mn is
483 trivalent. Natural feitknechtite samples typically include hausmannite, which presumably is an
484 alteration product of the feitknechtite. Feitknechtite occurs as an intermediate phase in syntheses
485 of birnessite by oxidation of $\text{Mn}(\text{OH})_2$ (Min and Kim 2019), and also has been reported in
486 biogenically precipitated Mn oxides (Mandernack et al. 1995). Polarized Raman spectra for
487 synthetic feitknechtite shown in Figure 20, and unpolarized spectra collecting using different
488 laser lines are compared in Figure 21.

489

490

491

492
493
494
495
496
497
498
499
500
501
502
503
504
505
506
507
508
509
510
511
512
513
514

DISCUSSION

Phase Identification

In a recent study, we concluded that when users employ appropriate data collection conditions, Raman spectroscopy is an effective tool for the identification and characterization of tunnel-structure Mn oxide phases (Post et al. 2020). The current work extends those conclusions to layer-structure Mn oxides. Raman spectra for the various layer structure Mn oxide phases are compared in Figure 22. As all phyllosulfates are constructed of similar MnO_6 octahedra, it is not surprising that there are general similarities among the spectra, especially in the region from ~ 300 to 665 cm^{-1} that is dominated by internal MnO_6 octahedra modes. The spectra have sufficiently unique characteristics, especially at frequencies below 500 cm^{-1} , to make it possible, in most cases, to identify specific phases. Additionally, the phyllosulfate spectra are distinctly different from large tunnel Mn oxide spectra (Fig. 23) as discussed below.

Recent studies have shown that Mn oxide minerals from a variety of nonmarine sources and in particular those assumed to form biogenically typically have layer or large-tunnel structures, or are mixtures of both (McKeown and Post 2001, Bargar et al 2009, Ling et al. 2020). Furthermore, laboratory experiments indicate that various environmental conditions transform phyllosulfates into tunnel structures, thereby significantly altering the reaction potentials for the Mn oxides in soils and sediments (Atkins et al. 2014, Grangeon et al. 2014, Yang et al. 2019). Routine Raman identification of specific tunnel or layer Mn oxides, even for fine-grained samples and mixtures, and surface coatings, can be critical to understanding and modeling their behaviors in a variety of natural settings.

515 The spectra plotted in Figure 23 suggest that a reliable method for distinguishing large
516 tunnel and layer structures is the presence or absence of a moderate-to-strong Raman mode near
517 $725\text{-}740\text{ cm}^{-1}$; this peak is present for all tunnel structures with predominantly Mn^{4+} , especially
518 for those with large tunnels, e.g. romanechite and todorokite, but is absent in all
519 phyllomanganate spectra – even layer structures containing only Mn^{4+} , such as chalcophanite.
520 This tunnel-structure marker peak is particularly strong when spectra are collected using 633 or
521 785 nm laser light. Post et al. (2020) suggested that this high frequency Mn-O stretch mode
522 arises from Mn^{4+} -O bonds in rigid octahedral tunnel structure frameworks. Phyllomanganate
523 octahedral sheets, on the other hand, are more elastic, softening the Mn-O stretches. This
524 behavior becomes even more pronounced with the replacement of some Mn^{4+} by the larger Mn^{3+}
525 or by vacancies.

526 As mentioned above, spectra collected from many phyllomanganates show strongly
527 polarized features, with strong intensities in the VV (laser light polarization parallel to analyzer
528 polarization direction) spectra, and weak intensities in the VH (laser light polarization
529 perpendicular to analyzer polarization direction) spectra. This behavior is particularly evident at
530 the highest frequencies that are dominated by internal MnO_6 octahedral motions. Spectra
531 collected under similar conditions for large-tunnel structures, however, showed little or no
532 polarization dependence (Post et al. 2020).

533

534 **Mn Oxidation State**

535 Post et al. (2020) concluded that Raman frequencies of certain internal MnO_6 octahedral
536 modes vary as a function of $\text{Mn}^{3+}/(\text{Mn}^{4+}+\text{Mn}^{3+})$ ratio. Increasing concentrations of the larger,
537 Jahn-Teller distorted Mn^{3+}O_6 octahedra cause a lengthening of the average Mn-O bond and a

538 more distorted octahedral environment, thereby decreasing the associated vibrational
539 frequencies. This is true in general for tunnel-structure Mn oxides, but is particularly true for the
540 hollandite group minerals, where a linear relationship was found between $Mn^{3+}/(Mn^{4+}+Mn^{3+})$
541 ratio and frequency of the internal MnO_6 octahedral mode near 630 cm^{-1} .

542

543 In the present study of phylломanganates, we similarly noted a strong linear correlation
544 ($R^2 = 0.984$) between the $Mn^{3+}/(Mn^{4+}+Mn^{3+})$ ratios and the frequencies for certain internal
545 MnO_6 octahedral modes (Fig. 24). The highest frequency mode for chalcophanite and ranciéite
546 occur near 669 cm^{-1} . This mode is dominated by internal MnO_6 octahedral vibrations, and might
547 be expected to appear at high frequencies for phases where all Mn is tetravalent. In contrast,
548 one-third of the Mn in triclinic Na- and K-birnessite is trivalent, and the comparable modes for
549 these phases were observed near 638 cm^{-1} . Cation exchange of triclinic Na-birnessite can
550 significantly alter the Mn redox state. For example, substitution of interlayer Na^+ with Ca^{2+}
551 (Elmi et al 2020) and H^+ (Sylvester et al. 1997) will significantly reduce the $Mn^{3+}/(Mn^{4+}+Mn^{3+})$
552 ratio (Ilton et al. 2016). In our Raman spectra of Ca- and H-birnessite, the internal MnO_6
553 octahedral mode peaks were shifted to higher frequencies relative to those for K-, Na-, and Li-
554 birnessites. The high-frequency modes plot approximately along the same trend line, with some
555 uncertainty arising from the broadness of the associated Raman peaks. Additionally, for certain
556 phases, some or all the Mn^{3+} will be in the interlayer region above or below octahedral
557 vacancies, and this different bonding environment will likely modify (broaden) some Raman
558 features.

559

560 The observed correlation of $\text{Mn}^{3+}/(\text{Mn}^{4+}+\text{Mn}^{3+})$ with the highest frequency Raman modes
561 suggests that Raman spectroscopy might be used to assess the approximate Mn^{3+} concentration
562 for birnessite-like phases, or for comparing Mn oxidation state before and after, or monitoring
563 during, certain types of reactions. It also offers the potential of using Raman spectroscopy to
564 map differences in Mn oxidation state in environmental or other complex samples.

565

566 **Birnessite Symmetry**

567 There has been considerable interest in recent years in establishing methods to distinguish
568 triclinic and hexagonal birnessite-like samples, as the structural symmetry correlates with the
569 Mn^{3+} and Mn site vacancy concentrations, which determine certain types of chemical
570 reactivities, and can be an indicator of the formation mechanism, e.g. biotic or abiotic (Tebo et
571 al. 2004, Webb et al. 2005). Commonly, powder X-ray diffraction patterns of natural birnessites
572 show only a few broad peaks resulting from small crystallite sizes or possibly long-range
573 structural disorder that cannot provide definitive long- or short-range symmetry characterization.
574 In recent years, some researchers used specific, although sometimes subtle, differences in X-ray
575 absorption spectroscopy features to distinguish triclinic from hexagonal birnessite-like phases
576 (e.g. Webb, 2005). Others use pair distribution function modeling to assess the symmetry and
577 other structural details (Yang et al. 2019; Lee et al. 2019). A drawback of both approaches is
578 that data must be collected using synchrotron sources. Additionally, the results are not always
579 conclusive, and in most cases *in situ* measurements are not routine.

580 Our results suggest that Raman spectroscopy offers several advantages for determining
581 the structural symmetry for birnessite-like phases. In addition to not requiring a synchrotron
582 source, Raman spectroscopy routinely enables the investigation of samples *in situ* with $\sim 1 \mu\text{m}$

583 spatial resolution. Moreover, several features robustly differentiate between the spectra for
584 triclinic (Na-birnessite) and hexagonal birnessite (H- birnessite) phases (Fig. 11). The internal
585 MnO_6 octahedral modes between 500 and 650 cm^{-1} correspond to at least three partially
586 resolved peaks in the Na-birnessite spectrum, and typically less resolved for H-birnessite. The
587 prominent, low-frequency peaks below 500 cm^{-1} in the Na-birnessite spectrum are absent or
588 significantly weaker, or shifted, for H-birnessite (Fig. 11). The position of the highest frequency
589 mode for Na-birnessite is shifted to lower frequency by approximately 10 cm^{-1} relative to that
590 for H-birnessite, reflecting the greater concentrations of Mn^{3+} in Na-birnessites. Additionally,
591 Figure 11 shows that the relative intensities for the two highest frequency modes (at about 580-
592 590 and 640-650 cm^{-1}) are reversed in the hexagonal and triclinic birnessites, as previously
593 observed by Julien et al. (2003), Hsu (2011), Yang et al. (2015), Boumaiza (2019), and
594 Bernardini (2019). These distinctly different spectra indicate that Raman spectroscopy, using the
595 appropriate data collection conditions, is perhaps the most conclusive method for readily
596 distinguishing triclinic from hexagonal birnessite. Furthermore, information derived from
597 Raman peak frequencies, relative intensities, and widths provide opportunities to explore
598 detailed structural variations among different birnessite-like phases beyond a simple triclinic or
599 hexagonal designation. Our results complement the study by Ling et al. (2017) that demonstrated
600 Fourier transform infra-red spectra effectively distinguish hexagonal and triclinic birnessite-like
601 structures, but Raman offers the advantages of better resolved spectral features and *in situ*
602 microanalyses.

603

604 **Vernadite**

605 Vernadite is reported as a major phase in ocean Mn nodules and crusts, and as indicated
606 above, is widely assumed to be a birnessite-like phase for which the basal reflection is largely
607 absent in powder X-ray diffraction patterns. The missing basal reflection is thought to arise
608 either from turbostratically disordered layer stacking, from crystallites with so few layers that
609 interference effects are minimized, or a combination of both of these factors. The phase is
610 characterized by a diffraction pattern showing broad peaks at ~ 2.44 and 1.45 \AA . Synthetic
611 samples that exhibit similar XRD patterns are commonly referred to as $\delta\text{-MnO}_2$ and are assumed
612 to be analogues of vernadite. The unpolarized Raman spectrum from an ocean Mn crust that
613 gave an XRD pattern consistent with vernadite is shown in Figure 25 along with spectra for
614 hexagonal birnessite, synthetic $\delta\text{-MnO}_2$, and asbolane. The natural vernadite spectrum most
615 closely resembles that for asbolane, or perhaps a mixture of asbolane and hexagonal birnessite,
616 and is distinctly different from that of $\delta\text{-MnO}_2$ (Villalobos et al. 2003), which is more similar to
617 that of hexagonal birnessite. This observation brings into question the assumption that $\delta\text{-MnO}_2$
618 is always an appropriate analogue for vernadite. The issue is complicated by the fact that there
619 are reported variations in composition, and presumably structures, for vernadites. In addition,
620 different synthesis methods and treatments have been employed to produce “ $\delta\text{-MnO}_2$ ” phases,
621 which are not always identical. Lee et al. (2019) concluded from their TEM and PDF studies of
622 ocean crust vernadite that this phase is best modeled by interstratified structures with 7 and 10 \AA
623 interlayer spacings. Our preliminary results suggest that Raman spectroscopy is a useful tool for
624 characterizing and comparing similarities and differences among natural vernadites and synthetic
625 $\delta\text{-MnO}_2$ phases. More in-depth Raman studies of a range of natural and synthetic vernadite-like
626 phases is ongoing.
627

628
629
630
631
632
633
634
635
636
637
638
639
640
641
642
643
644
645
646
647
648
649
650

IMPLICATIONS

We present here a comprehensive Raman spectroscopy study of layer structure Mn oxide phases from a large assortment of well-characterized natural and synthetic samples, using a variety of data collection conditions (Fig. 22). We demonstrate here and in our previous study of tunnel structure Mn oxides that when using multiple lasers, especially at 785 and 633 nm wavelengths, with low laser powers at the sample (30 – 500 μ W, depending upon the laser wavelength and the sample), we were able to consistently identify the Mn oxide phases for most samples. In particular, it is routinely possible to distinguish phases with large tunnels from those with layers (Fig. 23). Additionally, for birnessite-like phases, we observed that the position of the highest frequency Raman mode correlates with $\text{Mn}^{3+}/(\text{Mn}^{4+} + \text{Mn}^{3+})$, suggesting that Raman spectroscopy might be an effective tool for assessing approximate absolute and relative Mn^{3+} concentrations in this important group of phyllosulfates. With the comprehensive Raman database of well-characterized Mn oxide standards from Post et al (2020), and provided here and as supplementary data¹ with the *American Mineralogist*, micro-Raman is a powerful tool for identification and characterization of biotic and abiotic Mn oxide phases from diverse natural settings, and thereby can provide new insights into the roles of these phases in our environment and on other planets. Current plans for the next NASA Mars lander include a Raman system, where one of the primary targets will be black rock coatings that resemble rock varnishes on Earth (Marnocha 2017). As Mn oxides in terrestrial varnishes are thought to be biologically precipitated (McKeown and Post 2001; Northup et al. 2010; Marnocha and Dixon 2014), Raman identification of similar appearing Mn oxide minerals on Mars might be interpreted as indicators of past or possibly current biotic processes on Mars (Marnocha 2017). A comprehensive database of high-quality Raman spectra from well-characterized Mn oxide

651 minerals will be useful for such Martian studies. Additionally, the method is equally applicable
652 for identification and characterization of laboratory produced Mn oxides and those used
653 industrially.

654

655

656

657

ACKNOWLEDGEMENTS

658 We are grateful for the invaluable assistance provided by Rob Wardell with the operation
659 of the Raman laboratory in the Smithsonian Department of Mineral Sciences and Maxwell
660 Wetherington in the Raman laboratory of the Materials Characterization Laboratory, Penn State
661 University. Florence T. Ling kindly allowed us to analyze a suite of birnessite samples that she
662 synthesized. Funding for this work was provided by NSF Grant EAR-1925903

663

664

665

666

667

REFERENCES CITED

668

669 Atkins, A.L., Shaw, S., and Peacock, C.L. (2014) Nucleation and growth of todorokite
670 from birnessite: Implications for trace-metal cycling in marine sediments. *Geochimica et*
671 *Cosmochimica Acta*, 144, 109-125.

672 Bargar, J.R., Fuller, C.C., Marcus, M.A., Brearley, A.J., De la Rosa, M.P., Webb, S.M.
673 and Caldwell, W.A. (2009). Structural characterization of terrestrial microbial Mn oxides
674 from Pinal Creek, AZ. *Geochimica et Cosmochimica Acta*, 73, 889-910.

675 Bernard, M., Hugot-Le Goff, A., and Thi, B.V. (1993) Electrochromic reactions in
676 manganese oxides. *Journal of the Electrochemical Society*, 140, 3065-3070.

677 Bernardini, S., Bellatreccia, F., Municchia, A.C., Ventura, G.D., and Sodo, A. (2019)
678 Raman spectra of natural manganese oxides. *Journal of Raman Spectroscopy*, 1-16.

679 Betekhtin, A.,G. (1940) Southern Ural manganese deposits as a resource base for the
680 Magnitogorsk Metallurgical Trust, Trudi Institute of Geological Sciences. Academy of
681 Sciences. USSR. no. 4.

682 Boumaiza, H., Renard, A., Robinson, M.R., Kervern, G., Vidal, L., Ruby, C.,
683 Bergaoui, L., and Coustel, R. (2019) A multi-technique approach for studying Na triclinic
684 and hexagonal birnessites. *Journal of Solid State Chemistry*, 272, 234-243.

685 Bricker, O. (1965) Some stability relations in the system MnO_2 at 25° and one
686 atmosphere total pressure. *American Mineralogist*, 50, 1296-1354.

687 Burlet, C. and Vanbrabant, Y. (2015) Study of the spectro-chemical signatures of
688 cobalt–manganese layered oxides (asbolane–lithiophorite and their intermediates) by
689 Raman spectroscopy. *Journal of Raman Spectroscopy*, 46, 941-952.

690 Buser, W., Graf, P, and Feitkecht, W. (1954) Beitrag zur Kenntnis der Mangan(II)-
691 manganite und des δ -MnO₂. Helvetica chimica acta, 37, 2322-2333.

692 Chukhrov, F. V., Gorshkov, A. I., Rudnitskaya, Yeo S., et al. (1978) Vernadite.
693 Izvestiya AN SSSR, seriya geologicheskay a, 6, 5-19.

694 Chukhrov, F.V., Gorshkov, A.L., Vitovskaya, Lv. Drits, V.A. and Sntsov, A.V. (1982)
695 On the Nature of Co-Ni Asbolane; a Component of Some Supergene Ores. In Ore Genesis,
696 G. C. Amstutz et al. (eds.), Springer-Verlag Berlin Heidelberg, pp. 230-239.

697 Chukhrov, F.V., Drits, V.A., Gorshkov, A.I., Sakharov, B.A., and Dikov, Yu.P.
698 (1987) Structural models of vernadite. International Geology Review, 29, 1337-1347.

699 Dowty, E. (1987) "Vibrational interactions of tetrahedra in silicate glasses and
700 crystals", Physics and Chemistry of Minerals 14, 122-138.

701 Dowty, E. (2007) Vibratz2.0 software details available at: "www.shapesoftware.com".

702 Drits, V.A., Silvester, E., Gorshkov, A.I., and Manceau, A. (1997) Structure of
703 synthetic monoclinic Na-rich birnessite and hexagonal birnessite: I. Results from X-ray
704 diffraction and selected-area electron diffraction. American Mineralogist, 82, 946–961.

705 Elmi, C., Post, J.E., Heaney, P.J., and Ilton, E.S. (2020) Effects of pH and Ca
706 exchange on the structure and redox state of synthetic Na-birnessite. American
707 Mineralogist. In Press.

708 Ertle et al. (2005) Ertl, A., Pertlik, F., Prem, M., Post, J.E., Kim, S.J., Brandstatter, F.,
709 and Schuster, R. (2005) Ranciéite crystals from Friesach, Carinthia, Austria. European
710 Journal of Mineralogy, 17, 163–172.

711 Fateley, W.G., Dollish, F.R., McDevitt, N.T., and Bentley, F.F., Infrared and Raman
712 Selection Rules for Molecular and Lattice Vibrations: the Correlation Method, (Wiley,
713 New York, 1972).

714 Feng, X.H., Liu, F., Tan, W.F., and Liu, X.W. (2004) Synthesis of Birnessite from the
715 Oxidation of Mn^{2+} by O_2 in Alkali Medium: Effects of Synthesis Conditions. Clays and
716 Clay Minerals, 52(2), 240-250.

717 Feng, X.H., Zhai, L.M., Tan, W.F., Liu, F., and He, J.Z. (2007) Adsorption and redox
718 reactions of heavy metals on synthesized Mn oxide minerals. Environmental Pollution
719 147(2), 366-373.

720 Feng, M., Du, Q., Su, L., Zhang, G., Wang, G., Ma, Z., Gao, W., Qin, X., and Shao, G.
721 (2017) Manganese oxide electrode with excellent electrochemical performance for sodium
722 ion batteries by pre-intercalation of K and Na ions. Sci Rep, 7, 2219-2226.

723 Fischel, M.H., Fischel, J.S., Lafferty, B.J., and Sparks, D.L. (2015) The influence of
724 environmental conditions on kinetics of arsenite oxidation by manganese-oxides.
725 Geochemical Transactions, 16, 15-24.

726 Fischer, T.B., Heaney, P.J. and Post, J.E. (2018). Changes in the structure of birnessite
727 during siderophore-promoted dissolution: A time-resolved synchrotron X-ray diffraction
728 study. *Chemical Geology*, 476, 46-58.

729 Fleeger, C.R., Heaney, P.J., and Post, J.E. (2013) A time-resolved X-ray diffraction
730 study of Cs exchange into hexagonal H-birnessite. *American Mineralogist*, 98, 671-679.

731 Frey, C.E., Wiechen, M., and Kurz, P. (2014) Water-oxidation catalysis by synthetic
732 manganese oxides--systematic variations of the calcium birnessite theme. *Dalton*
733 *Transactions*, 43, 4370-4379.

734 Ghodbane, O., Pascal, J.L., and Favier, F. (2009) Microstructural effects on charge-
735 storage properties in MnO₂-based electrochemical supercapacitors. *Applied Materials &*
736 *Interfaces*, 2009. 1(5), 1130-1139.

737 Giovanoli, R. (1980) Vernadite is random-stacked birnessite. *Mineralium Deposita*,
738 14, 249-261.

739 Golden, D.C., Dixon, J.B., and Chen, C.C. (1986) Ion exchange, thermal
740 transformations, and oxidizing properties of birnessite. *Clays and Clay Minerals*, 34(5), 511-
741 520.

742 Grangeon, S., Lanson, B., Miyata, N., Tani, Y. and Manceau, A. (2010). Structure of
743 nanocrystalline phyllomanganates produced by freshwater fungi. *American Mineralogist*,
744 95, 1608-1616.

745 Grangeon, S., Manceau, A., Guilhermet, J., Gaillot, A., Lanson, M. (2012) Zn sorption
746 modifies dynamically the layer and interlayer structure of vernadite. *Geochimica et Cosmochimica*
747 *Acta*, 85, 302-313.

748 Grangeon S., Lanson B., and Lanson M. (2014) Solid-state transformation of
749 nanocrystalline phyllomanganate into tectomanganate: influence of initial layer and
750 interlayer structure. *Acta Crystallographica B*, 70, 828–838.

751 Grangeon, S., Warmont, F., Tournassat, C., Lanson, B., Lanson, M., Elkaïm, E., and
752 Claret, F. (2017). Nucleation and growth of feitknechtite from nanocrystalline vernadite
753 precursor. *European Journal of Mineralogy*, 29, 767-776.

754 Händel, M., Rennert, T., and Totsche, K.U. (2013) A simple method to synthesize
755 birnessite at ambient pressure and temperature. *Geoderma*, 193-194, 117-121.

756 Hinkle, M.A.G., Flynn, E.D., and Catalano, J.G. (2016) Structural response of
757 phyllomanganates to wet aging and aqueous Mn(II). *Geochimica Et Cosmochimica Acta*,
758 192, 220-234.

759 Hsu, Y. K., Chen, Y. C., Lin, Y. G., Chen, L. C., & Chen, K. H. (2011). Reversible
760 phase transformation of MnO₂ nanosheets in an electrochemical capacitor investigated by
761 in situ Raman spectroscopy. *Chemical Communications*, 47, 1252-1254.

762 Ilton, E.S., Post, J.E., Heaney, P.J., Ling, F.T. and Kerisit, S.N. (2016) XPS
763 determination of Mn oxidation states in Mn (hydr) oxides. *Applied Surface Science*, 366,
764 475-485.

765 Jiao, F., and Frei, H. (2010) Nanostructured manganese oxide clusters supported on
766 mesoporous silica as efficient oxygen-evolving catalysts. *Chem Commun (Camb)*, 46(17),
767 2920-2.

768 Jones, L.H.P., and Milne, A.A. (1956) Birnessite, a new manganese oxide mineral
769 from Aberdeenshire, Scotland. *Mineralogical Magazine*, 31, 283-288.

770 Julien, C., Massot, M., Baddour-Hadjean, R., Franger, S., Bach, S., and
771 Pereira-Ramos, J.P. (2003) Raman spectra of birnessite manganese dioxides. *Solid State*
772 *Ionics*, 159(3-4), 345-356.

773 Julien, C.M., Massot, M., and Poinسیون, C. (2004) Lattice vibrations of manganese
774 oxides. *Spectrochimica Acta Part A: Molecular and Biomolecular Spectroscopy*, 60(3),
775 689-700.

776 Kim, H. and Stair, P.C. (2004) Bacterially produced manganese oxide and todorokite:
777 UV Raman spectroscopic comparison, *Journal of Physical Chemistry B*, 108, 17019-
778 17026.

779 Kim, S.J. (1991) New characterization of takanelite. *American Mineralogist*, 76, 1426-
780 1430.

781 Kong, K.P., Fischer, T.B., Heaney, P.J., Post, J.E., Stubbs, J.E., and Eng, P.J. (2019).
782 Mineralogical and geochemical constraints on chromium oxidation induced by birnessite.
783 *Applied Geochemistry*, 108, 104365.

784 Kwon, K.D., Refson, K., and Sposito, G. (2013) Understanding the trends in transition
785 metal sorption by vacancy sites in birnessite. *Geochimica Et Cosmochimica Acta*, 101,
786 222-232.

787 Landrot, G., Ginder-Vogel, M., Livi, K., Fitts, J.P., and Sparks, D.L. (2012)
788 Chromium(III) oxidation by three poorly crystalline manganese(IV) oxides. 2. Solid phase
789 analyses. *Environ Sci Technol*, 46(21), 11601-9.

790 Lanson, B., Drits, V.A., Silvester, E., and Manceau, A. (2000) Structure of H-
791 exchanged hexagonal birnessite and its mechanism of formation from Na-rich monoclinic
792 busserite at low pH. *American Mineralogist*, 85, 826–838.

793 Lee, S., Xu, H., Xu, W., and Sun, X. (2019) The structure and crystal chemistry of
794 vernadite in ferromanganese crusts. *Acta Crystallographica*, B75, 591-598.

795 Le Goff, P., Baffier, N., Bach, S., and Pereira-Ramos, J.P. (1996) Synthesis, ion
796 exchange and electrochemical properties of lamellar phyllosulfates of the birnessite
797 group. *Materials Research Bulletin*, 31(1), 63-75.

798 Lefkowitz, J.P., Rouff, A.A., and Elzinga, E.J. (2013) Influence of pH on the reductive
799 transformation of birnessite by aqueous Mn(II). *Environmental Science & Technology*,
800 47(18), 10364-71.

801 Li, Z., Wang, J., Wang, Z., Ran, H., Li, Y., Han, X., and Yang, S. (2012) Synthesis of a
802 porous birnessite manganese dioxide hierarchical structure using thermally reduced

803 graphene oxide paper as a sacrificing template for supercapacitor application. New Journal
804 of Chemistry, 36(7), 1490-1495.

805 Ling, F.T., Post, J.E., Heaney, P.J., and Ilton, E.S. (2018) The relationship between
806 Mn oxidation state and structure in triclinic and hexagonal birnessites. Chemical Geology,
807 479, 216-227.

808 Ling, F.T., Post, J.E., Heaney, P.J., Kubicki, J.D., and Santelli, C.M. (2017) Fourier-
809 transform infrared spectroscopy (FTIR) analysis of triclinic and hexagonal birnessites.
810 Spectrochimica Acta Part A:Molecular and Biomolecular Spectroscopy, 178, 32-46.

811 Ling, F.T., Post, J.E., Heaney, P.J., Santelli, C.M., Ilton, E.S., Burgos, W.D., and
812 Rose, A.W. (2020) A multi-method characterization of natural terrestrial birnessites.
813 American Mineralogist, 105, 833-847.

814 Lopano, C.L., Heaney, P.J., Post, J.E., Hanson, J., and Komarneni, S. (2007) Time-
815 resolved structural analysis of K- and Ba-exchange reactions with synthetic Na-birnessite
816 using synchrotron X-ray diffraction. American Mineralogist, 92(2-3), 380-387.

817 Lopano, C.L., Heaney, P.J. and Post, J.E. (2009) Cs-exchange in birnessite: Reaction
818 mechanisms inferred from time-resolved X-ray diffraction and transmission electron
819 microscopy. American Mineralogist, 94, 816-826.

820 Lopano, C.L., Heaney, P.J., Bandstra, J.Z., Post, J.E., and Brantley, S.L. (2011)
821 Kinetic analysis of cation exchange in birnessite using time-resolved synchrotron X-ray
822 diffraction. Geochimica et Cosmochimica Acta, 75, 3973-3981.

823 Luo, J., Segal, S.R., Wang, J.Y., Tian, Z.R., and Suib, S.L. (1996). Synthesis,
824 characterization, and reactivity of feitknechtite. MRS Online Proceedings Library Archive,
825 431.

826 Manceau, A., Iorca, S.L., and Calas, G. (1987) Crystal chemistry of cobalt and nickel
827 in lithiophorite and asbolane from New Caledonia. *Geochimica et Cosmochimica Acta*,
828 51, 105-113.

829 Manceau, A., Lanson, B., and Drits, V.A. (2002) Structure of heavy metal sorbed
830 birnessite. Part III: Results from powder and polarized extended X-ray absorption fine
831 structure spectroscopy. *Geochimica Et Cosmochimica Acta*, 66(15), 2639-2663.

832 Mandernack, K.W., Post, J.E., and Tebo, B.M. (1995) Manganese mineral formation
833 by bacterial spores of the marine *Bacillus*, strain SG-1: evidence for the direct oxidation of
834 Mn (II) to Mn (IV). *Geochimica et Cosmchimica Acta*, 59, 4393-4408.

835 Manning, B.A., Fendorf, S.E., Bostick, B., and Suarez, D.L. (2002) Arsenic(III)
836 oxidation and arsenic(V) adsorption reactions on synthetic birnessite. *Environmental*
837 *Science & Technology*, 36(5), 976-81.

838 Marnocha, C.L. (2017) Rock coatings and the potential for life on Mars. *Elements*,
839 13, 187-191

840 Marnocha C.L. and Dixon J.C. (2014) Endolithic bacterial communities in rock
841 coatings from Kärkevagge, Swedish Lapland. *FEMS Microbiology Ecology* 90: 533-542

842 McKeown, D.A., and Post, J.E. (2001) Characterization of manganese oxide
843 mineralogy in rock varnish and dendrites using X-ray absorption spectroscopy. American
844 Mineralogist, 86, 701-713.

845 McKenzie, R.M. (1971) The Synthesis of birnessite, cryptomelane, and some other
846 oxides and hydroxides of manganese. Mineralogical Magazine, 38(296), 493-502.

847 Min, S. and Kim, Y. (2019). Phase transition and surface morphological characteristics
848 of Intermediate product feitknechtite according to aging time during the synthesis of
849 birnessite. Journal of the Mineralogical Society of Korea, 32, 213-222.

850 Nam, K.W., Kim, S., Yang, E., Jung, Y., Levi, E., Aurbach, D., and Choi, J.W. (2015)
851 Critical Role of Crystal Water for a Layered Cathode Material in Sodium Ion Batteries.
852 Chemistry of Materials, 27, 3721-3725.

853 Nambu, M. and Tanida, K. (1971) New mineral takanelite. The Journal of the
854 Japanese Association of Mineralogists, Petrologists and Economic Geologists, 65, 1-5.

855 Northup D.E. and 7 coauthors (2010) Diversity of rock varnish bacterial communities
856 from Black Canyon, New Mexico. Journal of Geophysical Research: Biogeosciences 115:
857 1-19

858 Ostwald, J. (1984) Two varieties of lithiophorite in some Australian deposits.
859 Mineralogical Magazine, 48. 383-388.

860 Post J.E. and Appleman D.E. (1988) Chalcophanite, $ZnMn_3O_7 \cdot 3H_2O$; new crystal-
861 structure determinations. American Mineralogist, 73, 1401–1404.

862 Post J.E. and Appleman D.E. (1994) Crystal structure refinement of lithiophorite.
863 American Mineralogist, 79, 370–374.

864 Post, J.E., Heaney, P.J., and Ertl, A. (2008) Rietveld refinement of the ranciéite
865 structure using synchrotron powder diffraction data. Powder Diffraction, 23(01), 10-14.

866 Post, J.E., Heaney, P.J., and Hanson, J. (2002) Rietveld refinement of a triclinic
867 structure for synthetic Na-birnessite using synchrotron powder diffraction data. Powder
868 Diffraction, 17(3), 218-221.

869 Post, J.E., McKeown, D.A., and Heaney, P.J. (2020) Raman Spectroscopy study of
870 Manganese Oxides – Tunnel Structures. American Mineralogist, In Press.

871 Post, J.E., and Veblen, D.R. (1990) Crystal structure determinations of synthetic
872 sodium, magnesium, and potassium birnessite using TEM and the Rietveld method.
873 American Mineralogist, 75, 477-489.

874 Post, J.E. (1999) Manganese oxide minerals: crystal structures and economic and
875 environmental significance. Proceedings of the National Academy of Sciences of the
876 United States of America, 96(7), 3447-54.

877 Santelli, C.M., Webb, S.M., Dohnalkova, A.C. and Hansel, C.M. (2011). Diversity of
878 Mn oxides produced by Mn (II)-oxidizing fungi. *Geochimica et Cosmochimica Acta*, 75,
879 2762-2776.

880 Sauer, K., and Yachandra, V.K. (2002) A possible evolutionary origin for the Mn⁴
881 cluster of the photosynthetic water oxidation complex from natural MnO₂ precipitates in
882 the early ocean. *Proceedings of the National Academy of Sciences of the United States of*
883 *America*, 99, 8631-8636.

884 Shannon, R.D. (1976) Revised Effective Ionic Radii and Systematic Studies of
885 Interatomic Distances in Halides and Chalcogenides. *Acta crystallographica. Section A*,
886 *Foundations of crystallography* 32, 751-767.

887 Shumlas, S.L., Singireddy, S., Thenuwara, A.C., Attanayake, N.H., Reeder, R.J., and
888 Strongin, D.R. (2016) Oxidation of arsenite to arsenate on birnessite in the presence of
889 light. *Geochemical Transactions*, 17, 5.

890 Silvester, E., Manceau, A. and Drits, V.A. (1997) Structure of synthetic monoclinic
891 Na-rich birnessite and hexagonal birnessite: II. Results from chemical studies and EXAFS
892 spectroscopy. *American Mineralogist*, **82**, 962-978.

893 Tan, H., Zhang, G.X., Heaney, P.J., Webb, S.M., and Burgos, W.D. (2010)
894 Characterization of manganese oxide precipitates from Appalachian coal mine drainage
895 treatment systems. *Applied Geochemistry*, 25(3), 389-399.

896 Tebo, B.M., Bargar, J.R., Clement, B.G., Dick, G.J., Murray, K.J., Parker, D., Verity,
897 R., and Webb, S. M. (2004). Biogenic manganese oxides: properties and mechanisms of
898 formation. *Annual Reviews in Earth and Planetary Science*, 32, 287-328.

899 Umena, Y., Kawakami, K., Shen, J. R. and Kamiya, N. (2011). Crystal structure of
900 oxygen-evolving photosystem II at a resolution of 1.9 Å. *Nature*, 473, 55-60.

901 Villalobos, Mario, Toner, B., Bargar, J., & Sposito, G. (2003). Characterization of the
902 manganese oxide produced by *Pseudomonas putida* strain MnB1. *Geochimica et*
903 *Cosmochimica Acta*, 67, 2649–2662.

904 Wang, M.X., Wang, Y.P., Tan, W.F., Liu, F., Feng, X.H., and Koopal, L.K. (2010)
905 Effect of 1-1 electrolyte concentration on the adsorption/desorption of copper ion on
906 synthetic birnessite. *Journal of Soils and Sediments*, 10(5), 879-885.

907 Webb, S.M., Tebo, B.M. and Bargar, J.R. (2005). Structural characterization of
908 biogenic Mn oxides produced in seawater by the marine *Bacillus* sp. strain SG-1. *American*
909 *Mineralogist*, 90, 1342-1357.

910 Wiechen, M., Zaharieva, I., Dau, H., and Kurz, P. (2012) Layered manganese oxides
911 for water-oxidation: alkaline earth cations influence catalytic activity in a photosystem II-
912 like fashion. *Chemical Science*, 3(7), 2330-2339.

913 Witzke, T., Pöllmann, H., Gardolinski, J.E.F.C. and Sommariva, M. (2017) Lagalyite,
914 IMA 2016, 106.

915 Yamaguchi, K., Shoji, M., Isobe, H., Yamanaka, S., Umena, Y., Kawakami, K. and
916 Kamiya, N. (2017) On the guiding principles for understanding of geometrical structures of
917 the CaMn₄O₅ cluster in oxygen-evolving complex of photosystem II. Proposal of
918 estimation formula of structural deformations via the Jahn–Teller effects. *Molecular*
919 *Physics*, 115, 636-666.

920 Yang, L.F., Cheng, S., Ji, X., Jiang, Y., Zhou, J., and Liu, M.L. (2015) Investigations
921 into the origin of pseudocapacitive behavior of Mn₃O₄ electrodes using in operando Raman
922 spectroscopy. *Journal of Materials Chemistry A*, 3(14), 7338-7344.

923 Yang, P., Post, J.E., Wang, Q., Xu, W., Geiss, R., McCurdy, P.R., and Zhu, M. (2019)
924 Metal adsorption controls stability of layered manganese oxides. *Environmental Science &*
925 *Technology* 53 (13), 7453-7462.

926 Yin, H., Liu, F., Feng, X., Hu, T., Zheng, L., Qiu, G., Koopal, L.K., and Tan, W.
927 (2013) Effects of Fe doping on the structures and properties of hexagonal birnessites –
928 Comparison with Co and Ni doping. *Geochimica et Cosmochimica Acta*, 117, 1-15.

929 Zhang, C., Chen, C., Dong, H., Shen, J. R., Dau, H. and Zhao, J. (2015) A synthetic
930 Mn₄Ca-cluster mimicking the oxygen-evolving center of photosynthesis. *Science*, 348,
931 690-693.

932 Zhao, H., Zhu, M., Li, W., Elzinga, E.J., Villalobos, M., Liu, F., Zhang, J., Feng, X.,
933 and Sparks, D.L. (2016) Redox Reactions between Mn(II) and Hexagonal Birnessite
934 Change Its Layer Symmetry. *Environmental Science & Technology*, 50(4), 1750-8.

935 Endnote: 1Deposit item AM-XXXX, Supplemental Material. Deposit items are free to
936 all readers and found on the MSA website, via the specific issue's Table of Contents (go to
937 http://www.minsocam.org/MSA/AmMin/TOC/20XX/XXXX_data/XXXX_data.html).

938

939

940

FIGURE CAPTIONS

941

942 **Figure 1.** Polyhedral drawings of manganese oxide layer structures. The blue octahedra contain
943 Mn; in chalcophanite, the green octahedra contain Zn, and for lithiophorite the magenta
944 octahedra are 2/3 Al and 1/3 Li. The yellow spheres in the birnessite structure represent
945 disordered Na atoms and water molecules.

946

947 **Figure 2.** Raman spectra (633 nm) for chalcophanite (NJ #C1814) with plate-like crystals (and
948 MnO₆ octahedral sheets) perpendicular to incident laser light direction. Spectra are labeled
949 Unpolarized (black), VV (blue), and VH (red). VV and VH spectra were collected using parallel
950 and crossed polarization conditions, respectively.

951

952 **Figure 3.** Raman spectra for chalcophanite (NJ #C1814) collected using 532 (0.03 mW), 633
953 (0.05 mW) and 785 (0.11 mW) nm laser light. Spectra are rescaled and offset for clarity.

954

955 **Figure 4.** Raman spectra (532 nm) for chalcophanite (NJ #C1814), ernienickelite (#171561), and
956 jianshuiite (MD) with plate-like crystals (and MnO₆ octahedral sheets) parallel to laser
957 polarization (laser light direction perpendicular to plate-like crystals).

958

959 **Figures 5a and b.** Raman spectra (532 nm) for: a) chalcophanite (NJ #C1814) with crystals
960 oriented with MnO₆ octahedral sheets parallel (top) and perpendicular (bottom) to the laser
961 polarization direction, and b) chalcophanite (NJ #C1814) and ernienickelite (#171561) showing

962 OH stretch modes with the polarization symbol indicating laser polarization perpendicular to the
963 MnO_6 octahedral sheets (or laser light direction parallel to MnO_6 octahedral sheets).

964

965 **Figure 6a and b.** a) Raman modes determined from lattice dynamics (LD) calculations for
966 chalcophanite (#C1814) plotted as vertical lines below their respective Raman spectra (633 nm),
967 and b) an eigenmode drawing of the highest calculated frequency A_g mode for chalcophanite:
968 (110) projection with the c-axis vertical, showing MnO_6 octahedral deformation, O-Mn-O bend
969 and Mn-O stretch, and Zn-O stretch with Zn translating along the c-axis.

970 **Figure 7.** Raman spectra (633 nm) for rancieite (#128319) with plate-like crystals (and MnO_6
971 octahedral sheets) perpendicular to incident laser light direction. Spectra labeled VV and VH
972 were collected using parallel and crossed polarization conditions, respectively.

973

974 **Figure 8.** Raman spectra for rancieite (#128319) collected using 532 (0.03 mW), 633 (< 0.1
975 mW) and 785 (0.11 mW) nm laser light. Spectra are rescaled and offset for clarity.

976

977 **Figure 9.** Raman spectra (785 nm) for a variety of different rancieite specimens. Locations and
978 specimen numbers are indicated (see Table 1). Samples were flattened such that MnO_6
979 octahedral sheets were perpendicular to incident laser light direction. Spectra are rescaled and
980 offset for clarity.

981

982 **Figure 10.** Raman modes determined from LD calculations for rancieite (#128319) plotted as
983 vertical lines below their respective Raman spectra (633 nm laser light).

984

985 **Figure 11a. and b.** Raman spectra for synthetic triclinic Na-birnessite and synthetic hexagonal
986 birnessite, with plate-like crystals (and MnO₆ octahedral sheets) perpendicular to incident laser
987 light direction, using a) 633 nm and b) 785 nm laser light. Spectra are rescaled and offset for
988 clarity.

989
990 **Figure 12a. and b.** a) Raman spectra for Na-birnessite collected using 532 (0.03 mW), 633 (<
991 0.1 mW) and 785 (0.11 mW) nm laser light, and b) Raman spectra (633 nm) for Na-birnessite
992 using different laser power levels at the sample (each measurement was from a different, but
993 nearby point on the sample). Sample alteration is evident at incident powers above 0.1 mW.
994 Sample alteration at 0.15 mW can result in different mixtures of phases as shown for two
995 different points on the sample. Spectra are rescaled and offset for clarity.

996
997 **Figure 13.** Na-birnessite Raman modes determined from LD calculations for the simplified
998 C2/m monoclinic structure plotted as vertical lines below their respective Raman features in the
999 785 nm spectrum.

1000
1001 **Figure 14.** Raman spectra (785 nm) for a variety of synthetic birnessite specimens with different
1002 interlayer cations (see Table 1). Samples were flattened such that MnO₆ octahedral sheets were
1003 perpendicular to incident laser light direction. Spectra are rescaled and offset for clarity.

1004

1005

1006 **Figure 15.** Raman spectra (633 nm) for vernadite (Pacific ocean crust), with plate-like crystals
1007 (and MnO₆ octahedral sheets) perpendicular to incident laser light direction. Spectra labeled VV
1008 and VH were collected using parallel and crossed polarization conditions, respectively.

1009

1010

1011 **Figure 16.** Polarized Raman spectra (514.5 nm) for lithiophorite (#162391), with plate-like
1012 crystals (and MnO₆ octahedral sheets) perpendicular to incident laser light direction and parallel
1013 to the laser polarization. Spectra labeled VV and VH were collected using parallel and crossed
1014 polarization conditions, respectively.

1015

1016 **Figure 17.** Raman spectra for lithiophorite (#162391) collected using 532 (0.03 mW), 633 (< 0.1
1017 mW) and 785 (0.11 mW) nm laser light. Spectra are rescaled and offset for clarity.

1018

1019 **Figure 18.** Raman modes determined using lattice dynamics (LD) calculations for lithiophorite
1020 (#162391) structure; the calculated mode frequency for each mode is plotted as a vertical line
1021 below their respective Raman spectra (514.5 nm laser light).

1022

1023 **Figure 19.** Raman spectra (785 nm laser light) for a variety of different asbolane specimens
1024 (Table 1). The Co/Mn (Table 1) in the samples increases from the top to bottom spectrum.
1025 Spectra are rescaled and offset for clarity.

1026

1027 **Figure 20.** Raman spectra (633 nm) for synthetic feitknechtite. Spectra labeled VV and VH
1028 were collected using parallel and crossed polarization conditions, respectively.

1029

1030 **Figure 21.** Raman spectra for feitknechtite collected using 532 (0.03 mW), 633 (< 0.1 mW) and
1031 785 (0.11 mW) nm laser light. Spectra are rescaled and offset for clarity.

1032

1033 **Figure 22.** Raman spectra for a variety of phylломanganates, ordered from top to bottom
1034 according to decreasing $Mn^{3+}/(Mn^{4++}Mn^{3+})$. Specimens measured are: chalcophanite
1035 (R12334), rancieite Austria, synthetic Ca-birnessite, synthetic Na-birnessite, synthetic hexagonal
1036 birnessite, and lithiophorite (162391) (Table 1). Spectra are rescaled and offset for clarity.

1037

1038 **Figure 23.** Raman spectra for a variety of layer- and tunnel-structure Mn oxide phases. Tunnel
1039 structure Mn-oxide spectra originally presented in the tunnel Mn-oxide study, Post et al. (2020);
1040 samples: cryptomelane (NMNH 89104), romanechite (NMNH R2232), todorokite (HU 126232).
1041 Layer structure spectra from: chalcophanite (R12334), rancieite Austria, synthetic Na-birnessite,
1042 synthetic hexagonal birnessite, and lithiophorite (162391). Spectra are rescaled and offset for
1043 clarity.

1044

1045 **Figure 24.** $Mn^{3+}/(Mn^{3+}+Mn^{4+})$ ratio versus Raman shift frequency of the highest frequency
1046 vibrational mode for the different phylломanganates included in this study.

1047

1048 **Figure 25.** Raman spectra (785 nm) for vernadite (Pacific ocean crust), asbolane (#103709),
1049 synthetic hexagonal birnessite (pH 2), and synthetic δ -MnO₂. Spectra are rescaled and offset for
1050 clarity.

1051

1052

1053

1054

1055

1056

1057

1058

1059 **Table 1 Specimens used for Raman Spectroscopy**

Mineral	Specimen #	Locality	Chemical Formula
Chalcophanite	C1814	Sterling Hill mine, NJ	ZnMn ₃ O ₇ · 3H ₂ O
	R12334	Bisbee, AZ	ZnMn ₃ O ₇ · 3H ₂ O
Ernienickelite	171561	Kalgoorlie-Boulder Shire, Australia	NiMn ₃ O ₇ · 3H ₂ O
Jianshuiite		Medford Quarry, MD	MgMn ₃ O ₇ · 3H ₂ O

Rancieite		Friesach, Austria	$\text{Ca}_{0.19}\text{K}_{0.01}(\text{Mn}^{4+}_{0.91}\square_{0.09})\text{O}_2 \cdot 0.63\text{H}_2\text{O}$
	128318	Rancie Mtn., France	$\text{Ca}_{0.14}\text{Mg}_{0.04}\text{Ba}_{0.01}\text{K}_{0.01}(\text{Mn}^{4+}_{0.87}\text{Zn}_{0.06}\square_{0.07})\text{O}_2 \cdot 0.63\text{H}_2\text{O}$
	29.74	Alsace, France	$\text{Ca}_{0.16}\text{Mg}_{0.01}\text{Ba}_{0.01}\text{K}_{0.01}(\text{Mn}^{4+}_{0.91}\square_{0.09})\text{O}_2 \cdot 0.63\text{H}_2\text{O}$
		Spain	$\text{Ca}_{0.13}\text{Mg}_{0.04}\text{Ba}_{0.02}\text{K}_{0.01}(\text{Mn}^{4+}_{0.91}\square_{0.09})\text{O}_2 \cdot 0.63\text{H}_2\text{O}$
Na-birnessite		Synthetic ^a	$\text{Na}_{0.58}(\text{Mn}^{4+}_{1.34}\text{Mn}^{3+}_{0.66})\text{O}_4 \cdot 1.4\text{H}_2\text{O}$
K-birnessite		Synthetic ^a	$\text{K}_{0.58}(\text{Mn}^{4+}_{1.34}\text{Mn}^{3+}_{0.66})\text{O}_4 \cdot 1.4\text{H}_2\text{O}$
Li-birnessite		Synthetic ^a	$\text{Li}_{0.58}(\text{Mn}^{4+}_{1.34}\text{Mn}^{3+}_{0.66})\text{O}_4 \cdot 1.4\text{H}_2\text{O}$
Ba-birnessite		Synthetic ^a	$\text{Ba}_{0.29}(\text{Mn}^{4+}_{1.34}\text{Mn}^{3+}_{0.66})\text{O}_4 \cdot 1.6\text{H}_2\text{O}$
Ca-birnessite		Synthetic ^a	$\text{Ca}_{0.30}(\text{Mn}^{4+}_{1.34}\text{Mn}^{3+}_{0.50}\square_{0.16})\text{O}_4 \cdot 1.6\text{H}_2\text{O}$
Hex-birnessite		Synthetic (pH 2) ^b	$\text{Mn}^{3+}_{0.2}(\text{Mn}^{4+}_{1.34}\text{Mn}^{3+}_{0.66}\square_{0.09})\text{O}_4 \cdot 1.6\text{H}_2\text{O}$
Vernadite		Pacific Ocean crust	$\text{Na}_{0.47}\text{Ca}_{0.28}\text{Mg}_{0.16}\text{K}_{0.03}(\text{Fe}_{1.18}\text{Si}_{2.8}\text{Al}_{0.7}\text{Ti}_{0.09}\square)(\text{Mn}^{4+}, \text{Mn}^{3+})_2\text{O}_4 \cdot n\text{H}_2\text{O}$
δ -MnO ₂		Synthetic ^c	$(\text{Na}_{0.09}\text{Mn}^{3+}_{0.08}\text{K}_{0.07})(\text{Mn}^{4+}_{0.70}\text{Mn}^{3+}_{0.26}\square_{0.04})\text{O}_2 \cdot n\text{H}_2\text{O}$
Feitknechtite ^d		Synthetic	Mn(OH) ₃ (assumed)
Lithiophorite	162391	Postmasburg, South Africa	$(\text{Al}_{0.67}\text{Li}_{0.33})(\text{Mn}^{4+}_{0.67}\text{Mn}^{3+}_{0.33})\text{O}_2(\text{OH})_2$
		Georgia, USA	$(\text{Al}_{0.80}\text{Co}_{0.08})(\text{Mn})\text{O}_2(\text{OH})_x$
	46158	Rengersdorf, Germany	$(\text{Al}_{0.75}\text{Si}_{0.09}\text{Co}_{0.06}\text{Ni}_{0.03})\text{MnO}_2(\text{OH})_x$
Asbolane	97579	Kasaigaigori, Japan	$(\text{Al}_{0.79}\text{Co}_{0.34}\text{Fe}_{0.04})\text{MnO}_2(\text{OH})_x$

	103709	La Motte mi., Missouri	$(\text{Co}_{.69}\text{Cu}_{.24}\text{Ni}_{.10}\text{Zn}_{.04}\text{Al}_{.04})\text{MnO}_2(\text{OH})_x$
	R2247	Sachsen, Germany	$(\text{Al}_{.78}\text{Co}_{.14}\text{Fe}_{.22})\text{MnO}_2(\text{OH})_x$
	R9752	Schneeberg, Germany	$(\text{Al}_{.47}\text{Co}_{.04}\text{Fe}_{.05})\text{MnO}_2(\text{OH})_x$

1060 a – Na-birnessite synthesized and sample exchanged with respective interlayer cation following
1061 method of Golden et al (1986)

1062 b – Hexagonal birnessite formed by reacting Na-birnessite with pH 2 HCl solution.

1063 c – sample provided by M. Zhu, synthesized using method of Villilobos et al. (2003)

1064 d – sample provided by E. Elzinga

1065 Note: Li content for lithiophorite from South Africa determined by single crystal X-ray structure
1066 refinement by Post and Appleman (1994); Li concentrations were not determined for other
1067 lithiophorite and asbolane samples. Asbolane cation values were normalized to one Mn.

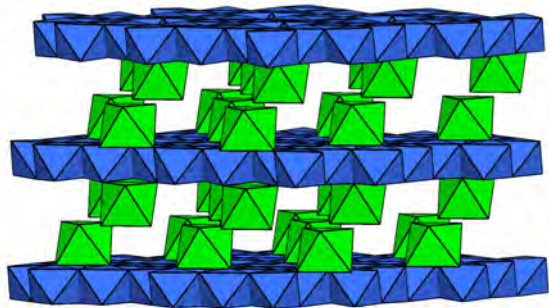
1068

1069

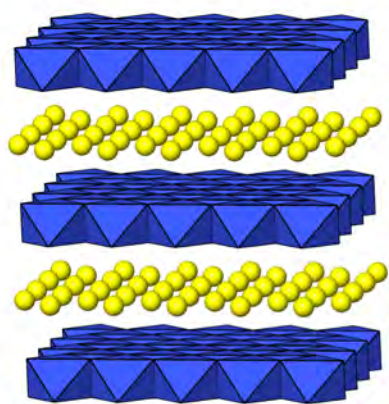
1070 Table 2. Factor group analysis (FGA) results of the tunnel structure-type Mn-oxides phases. Γ_{optic}
 1071 includes Raman- and IR-active modes; three Γ_{acoustic} modes are indicated for each phase. The
 1072 space group of each phase are listed in Hermann-Mauguin notations.

<u>Phase</u>	<u>Space Group:</u>	<u>FGA</u>	1073
Lithiophorite	R-3m (#166)	$\Gamma = 3A_{1g} + 3E_g + 5A_{2u} + 5E_u$	1074
		$\Gamma_{\text{Acoustic}}: A_{2u}(z) + E_u(xy)$	1075
			1076
Chalcophanite	R-3 (#148)	$\Gamma = 14A_g + 14E_g + 14A_u + 14E_u$	1077
		$\Gamma_{\text{Acoustic}}: A_u(z) + E_u(xy)$	1078
			1079
Na-Birnessite	C-1 (#2)	$\Gamma = 6A_g + 6A_u$	1080
		$\Gamma_{\text{Acoustic}}: 3A_g$	1081
Rancieite	P -3	$\Gamma = 5A_g + 5E_g + 5A_u + 5E_u$	
		$\Gamma_{\text{Acoustic}}: A_u + E_u$	

Chalcophanite



Na-Birnessite



Lithiophorite

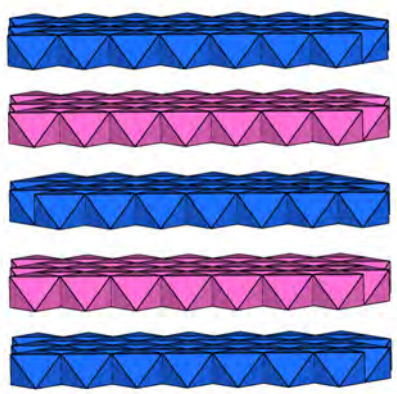


Figure 1

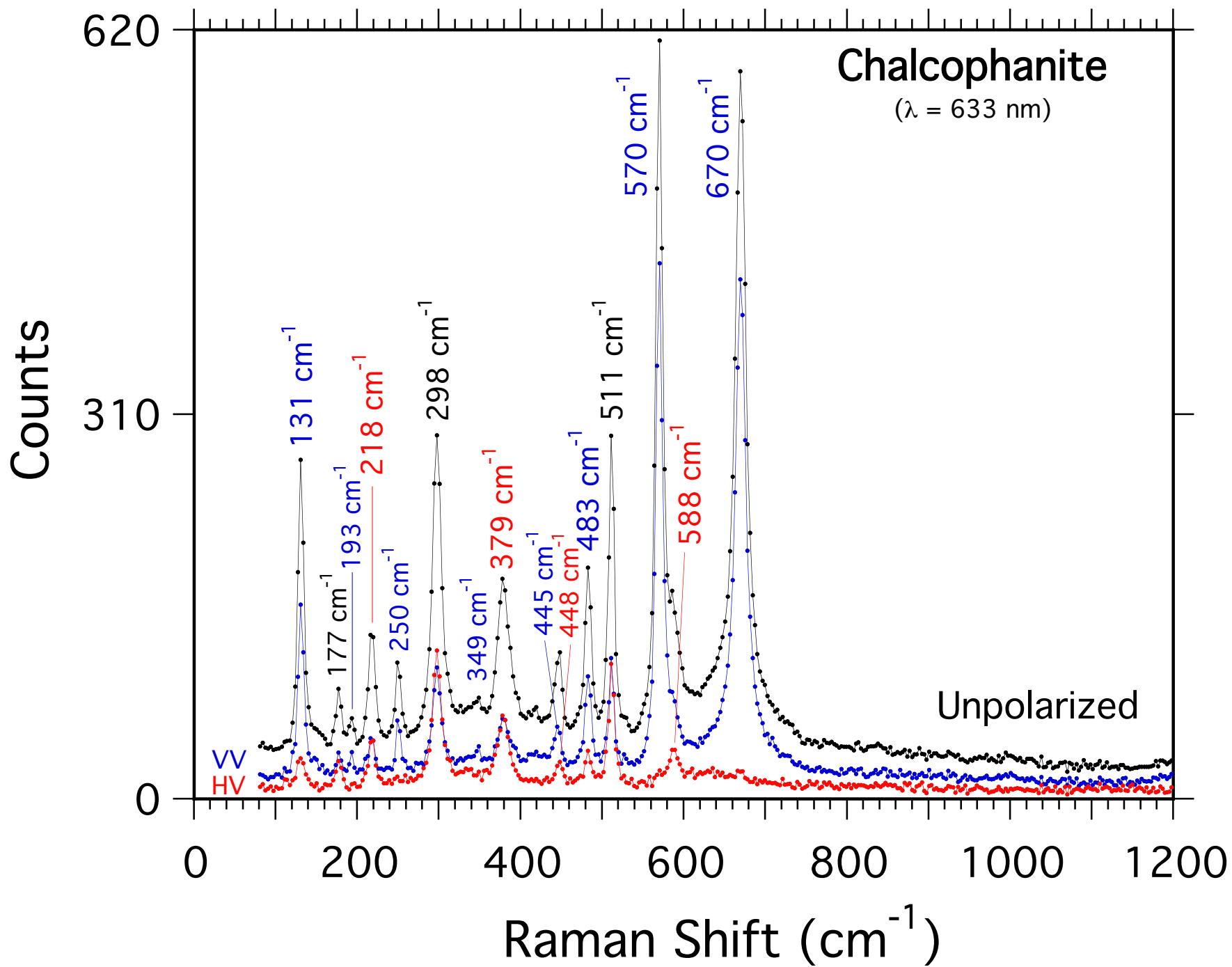


Fig. 2

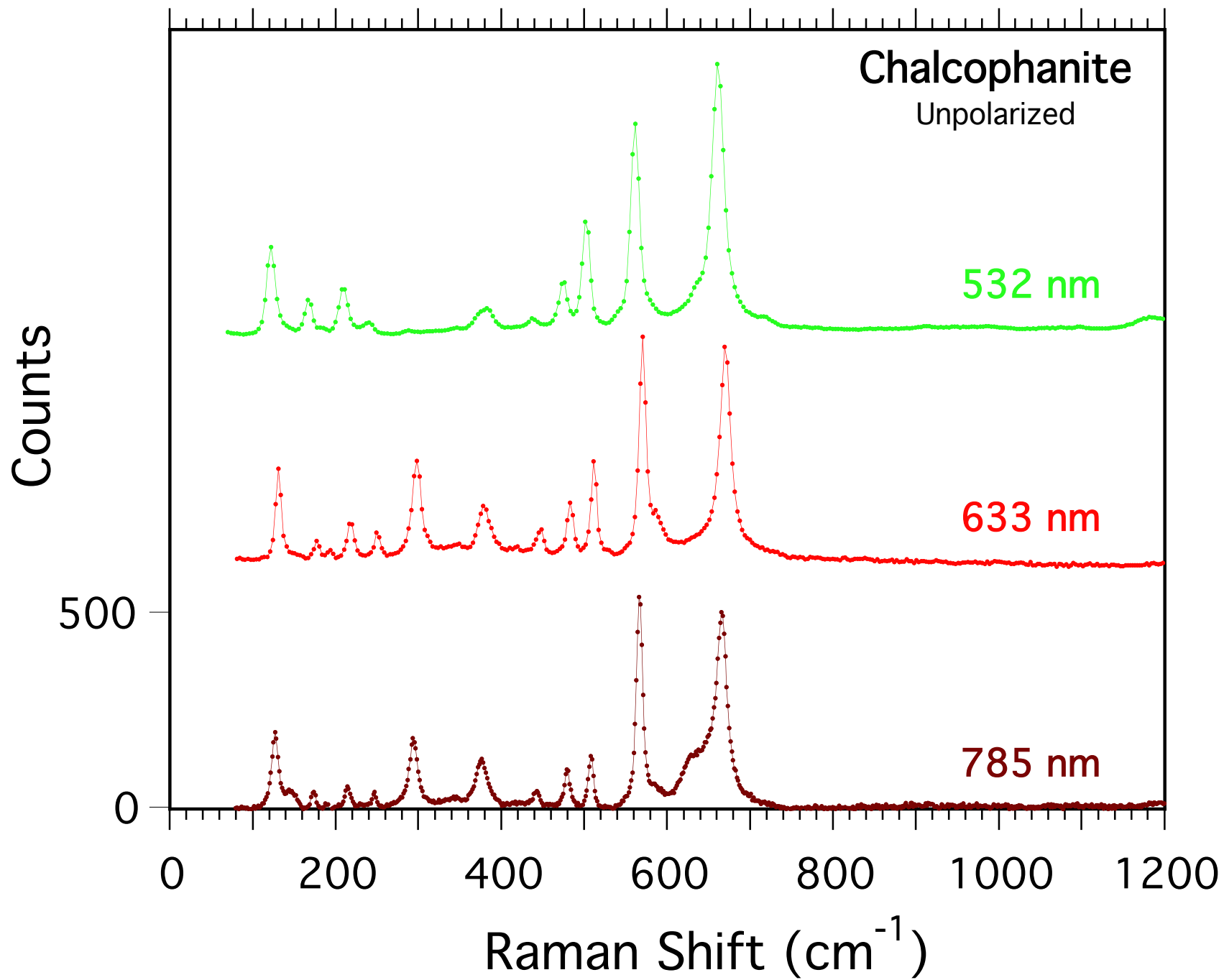


Fig. 3

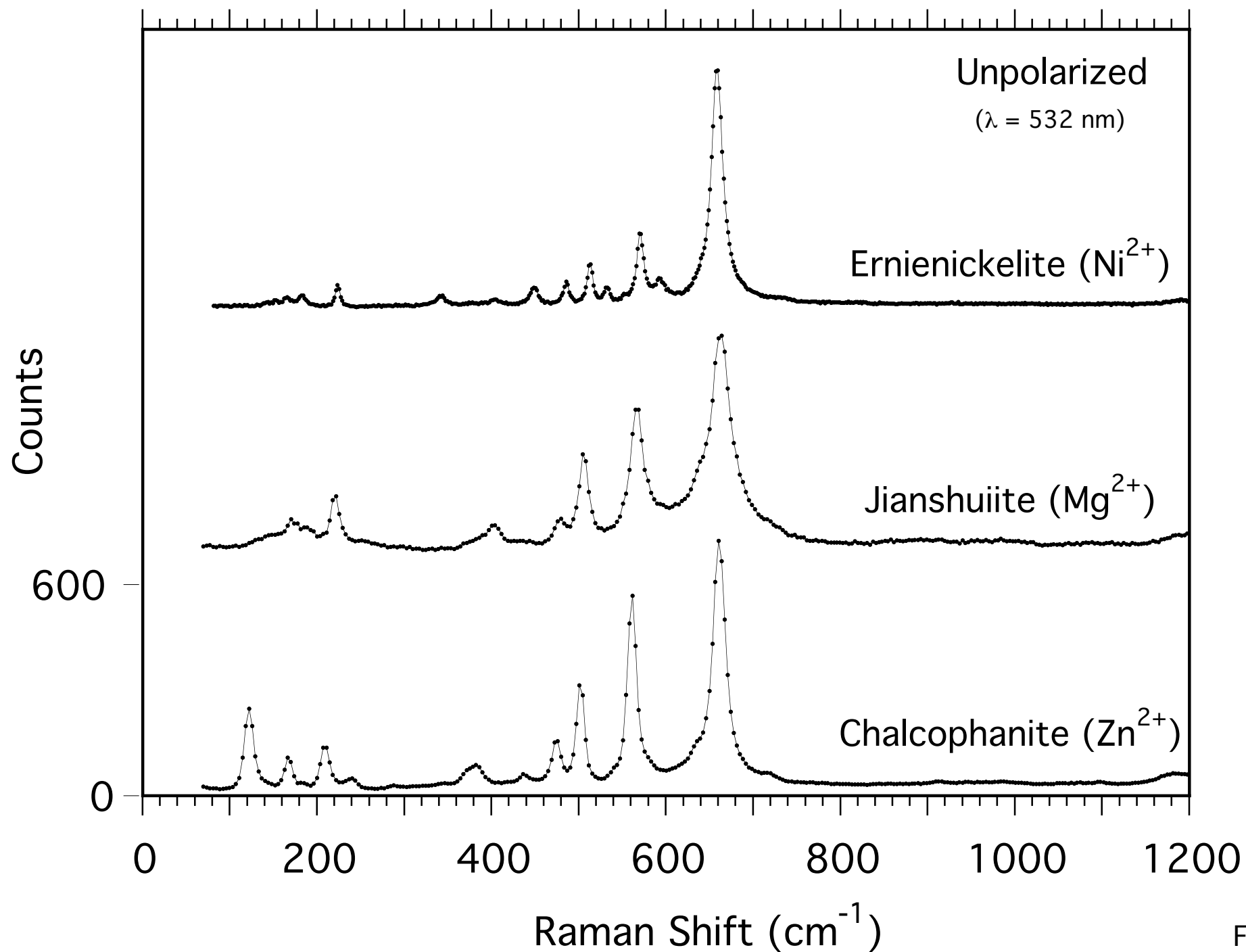


Fig. 4

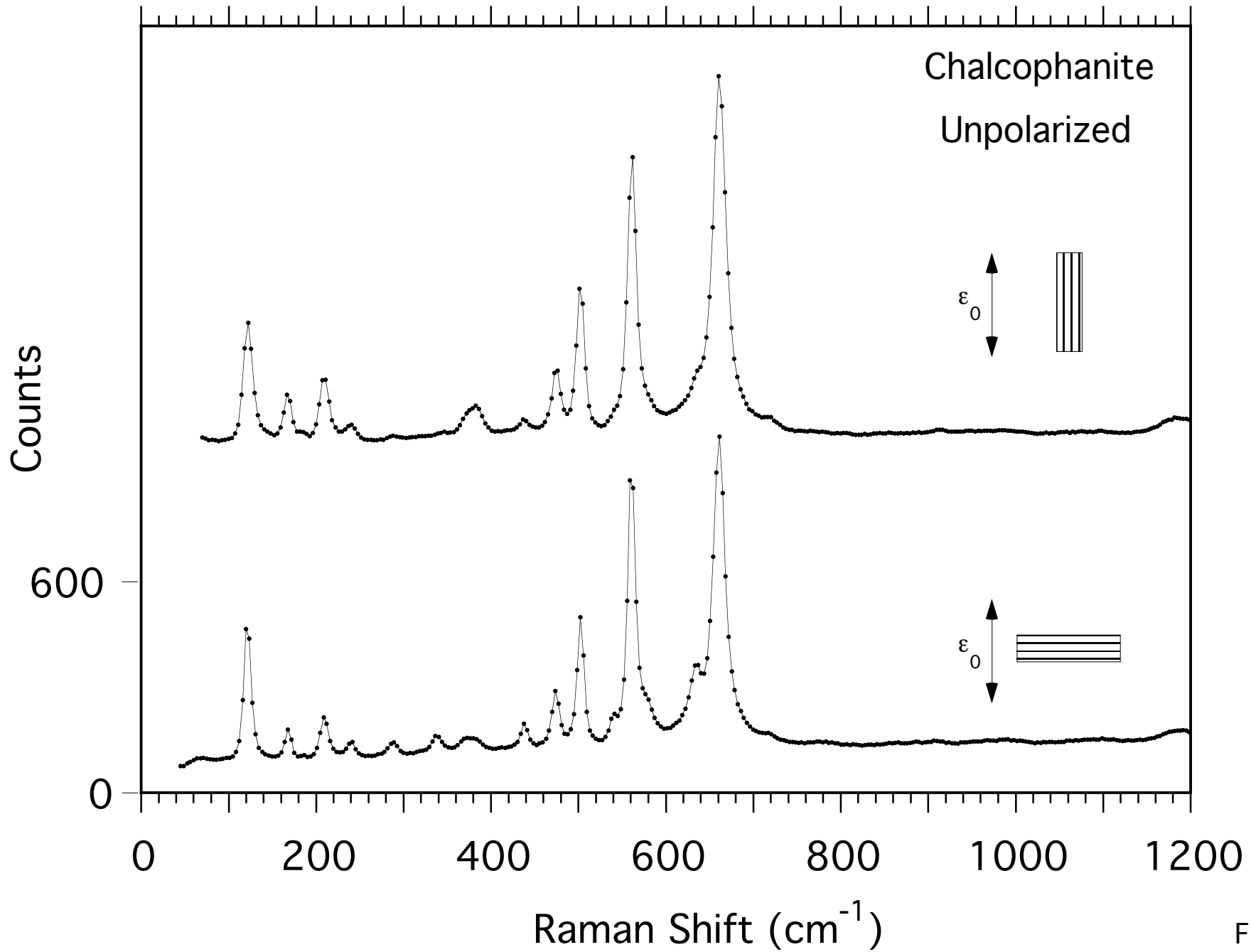


Fig. 5a

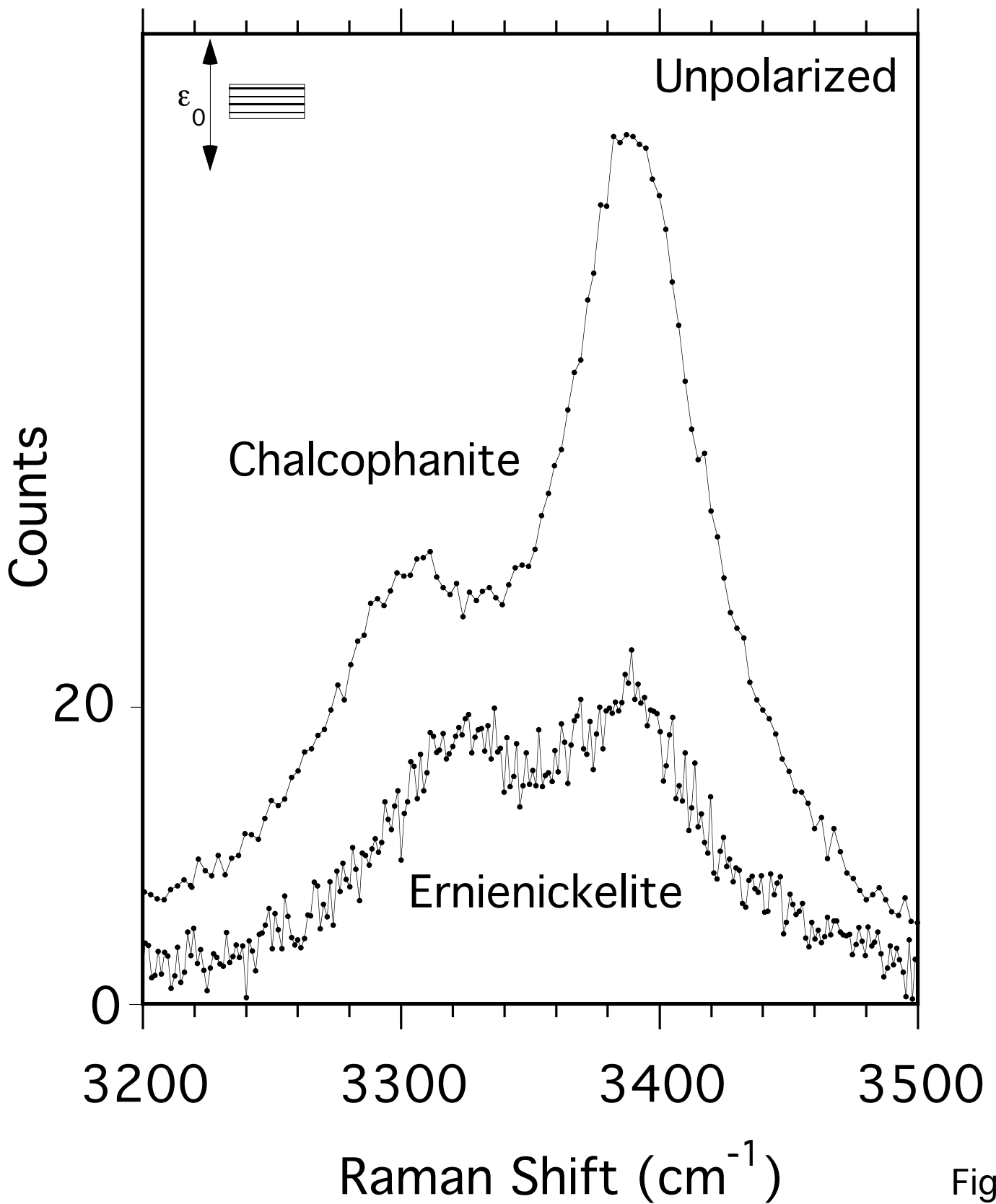


Fig. 5b

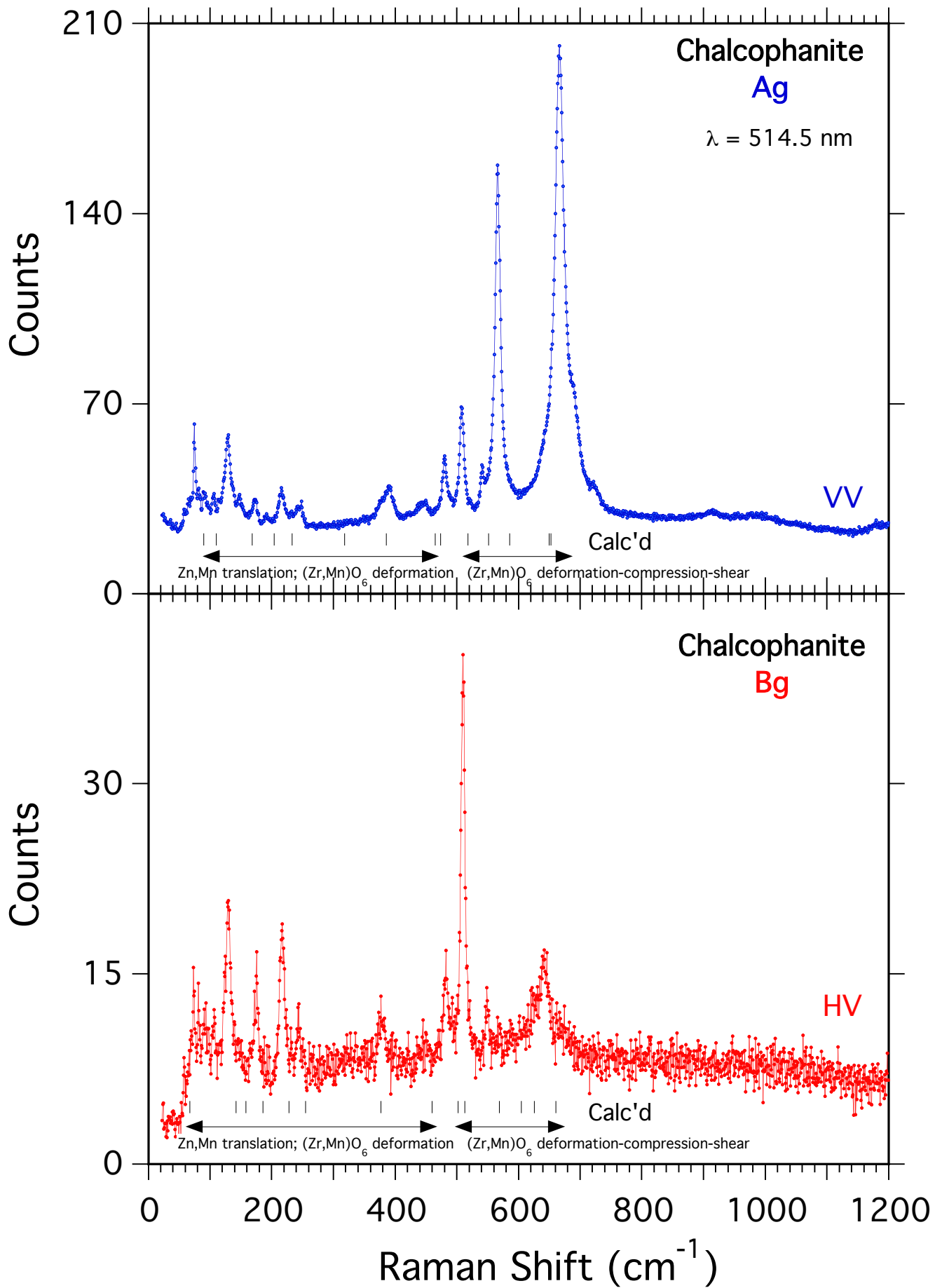


Fig. 6a

Chalcophanite
 $653\text{ cm}^{-1}\text{ Ag}$

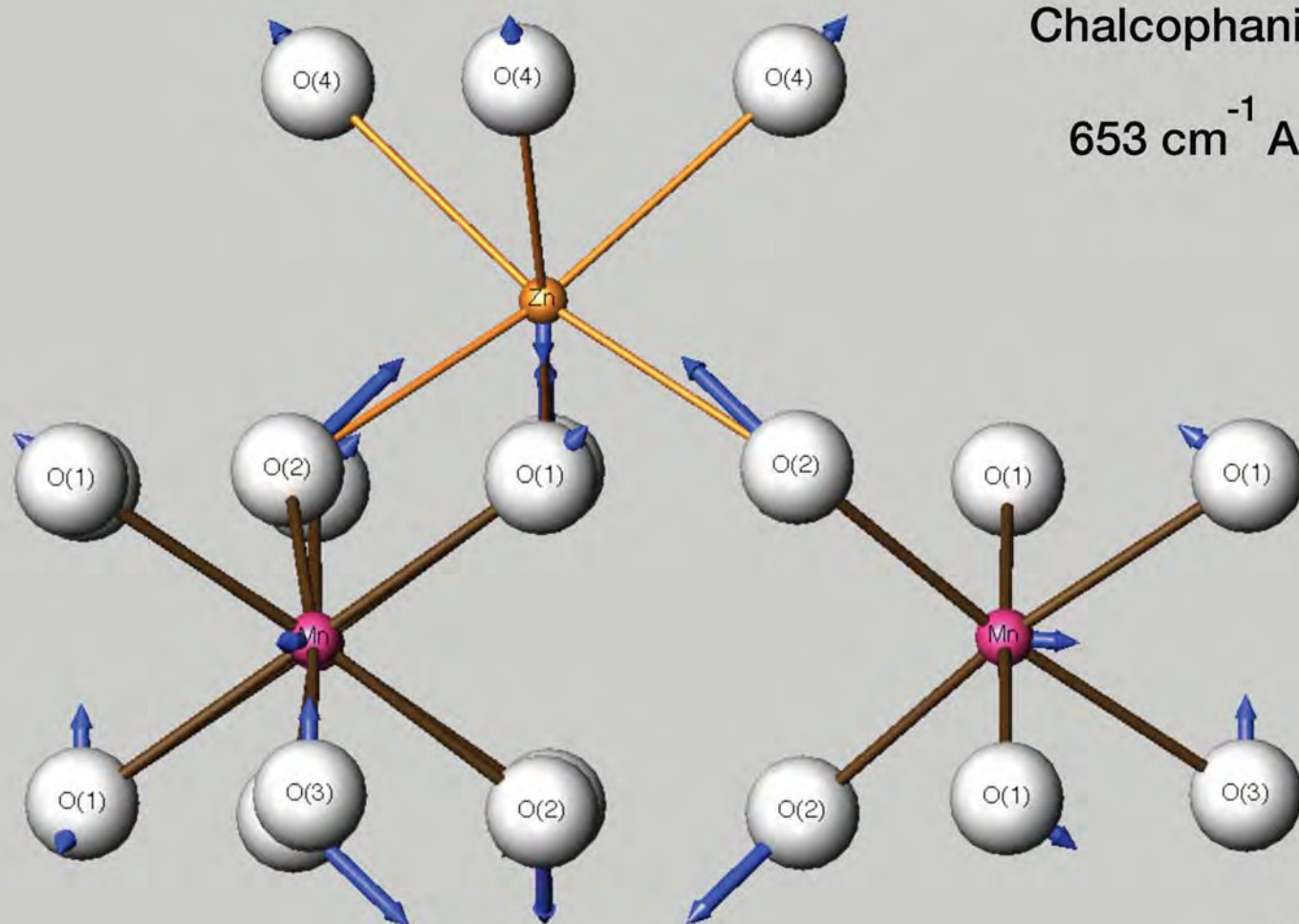


Fig. 6b

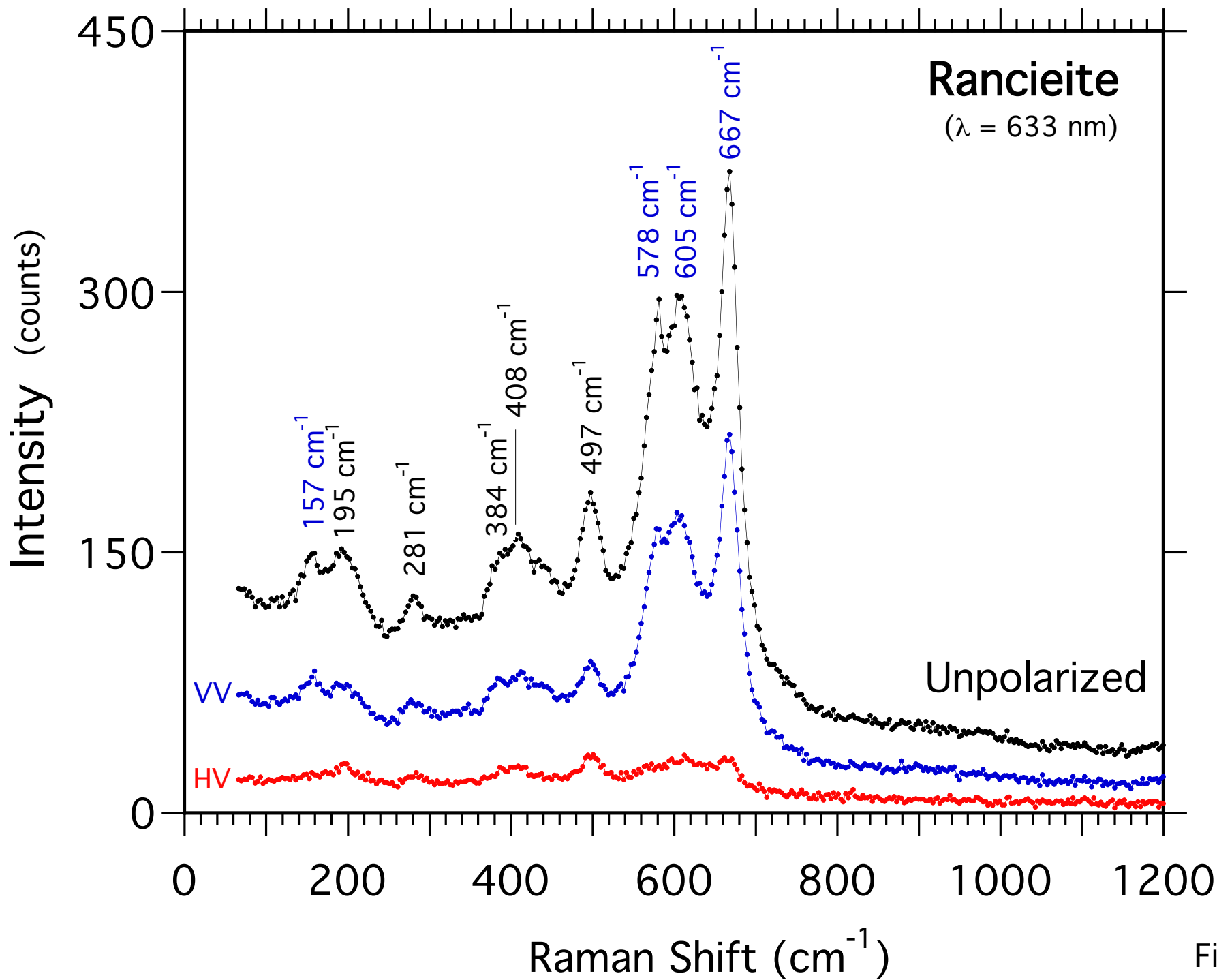


Fig. 7

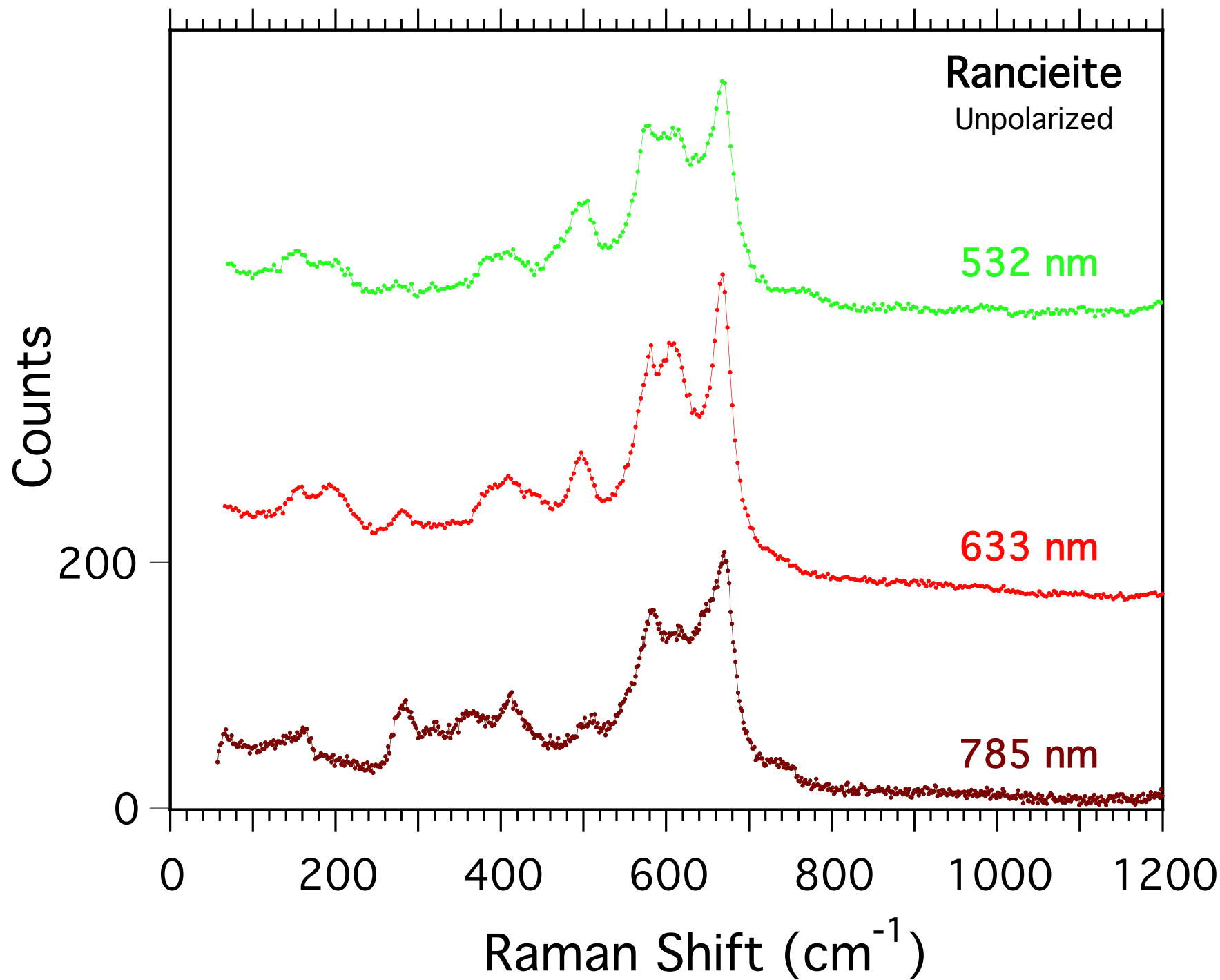


Fig. 8

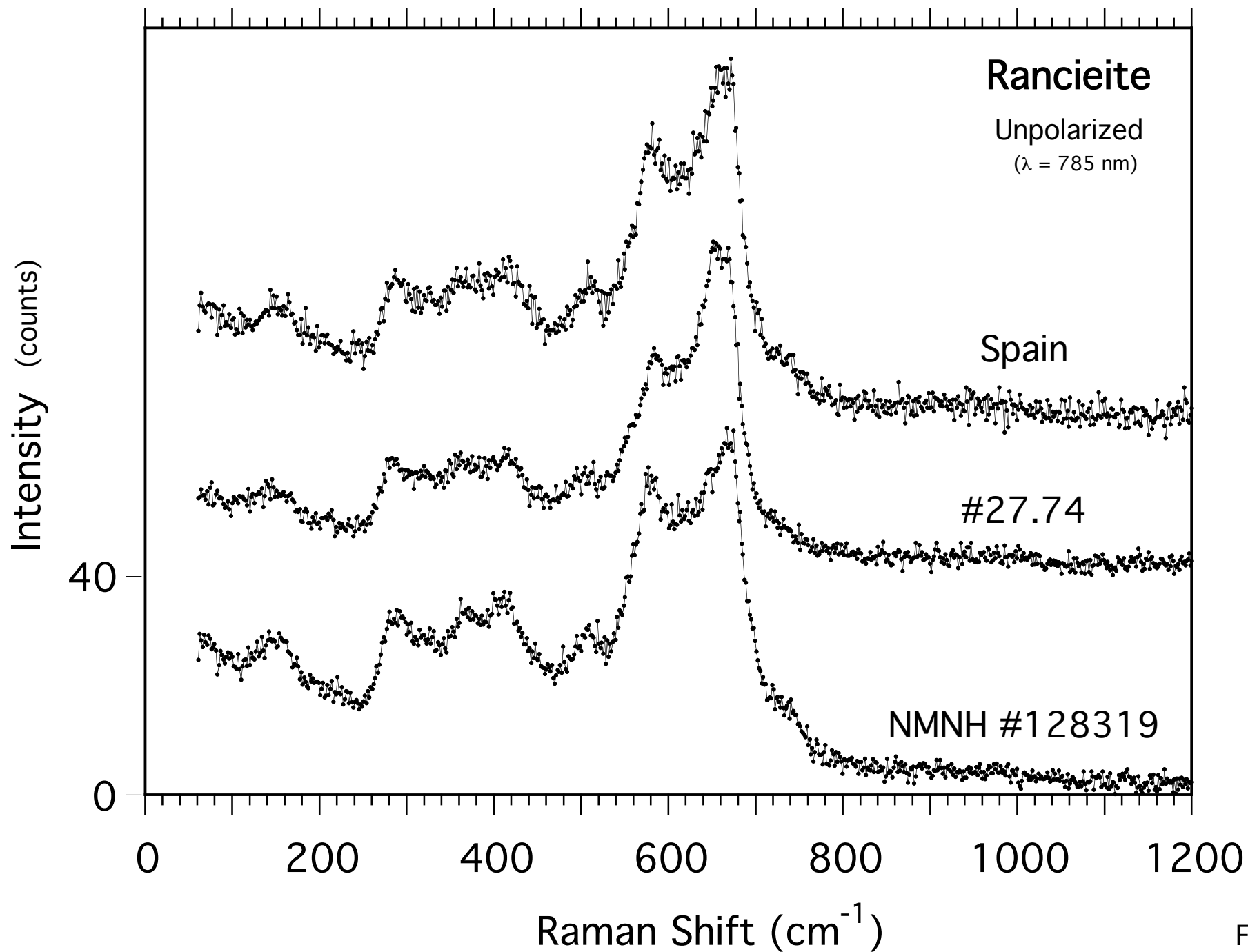


Fig. 9

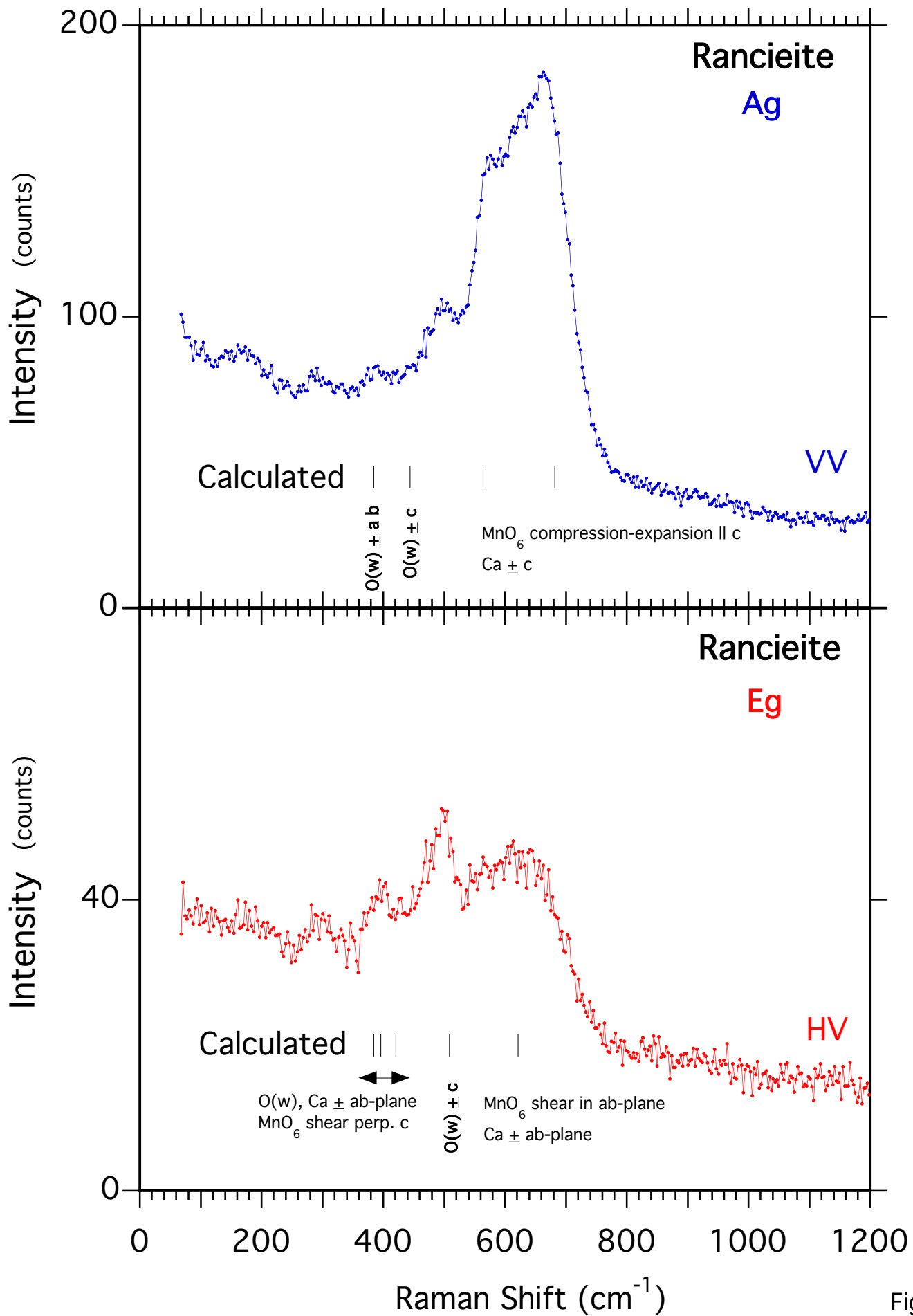


Fig. 10

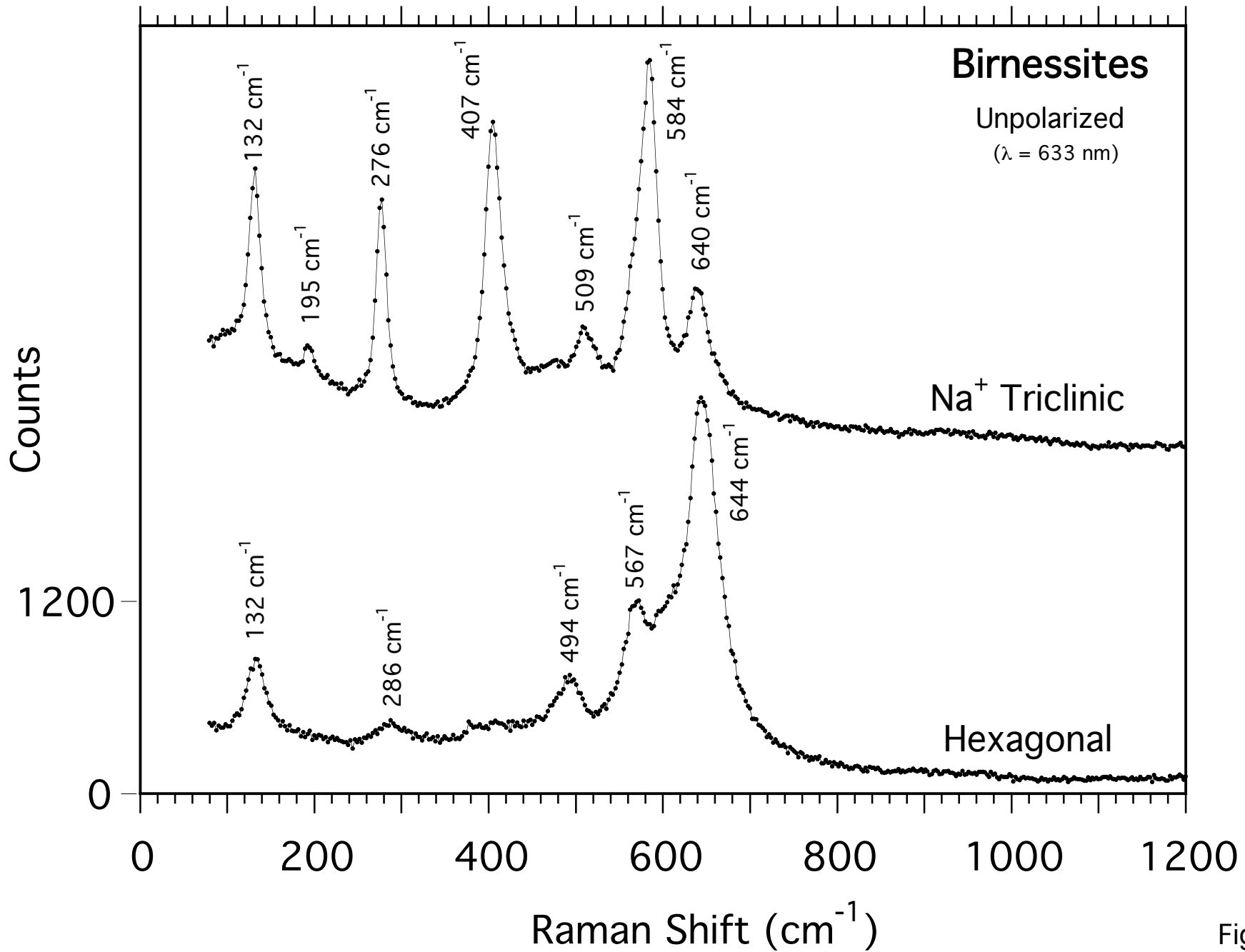


Fig. 11a

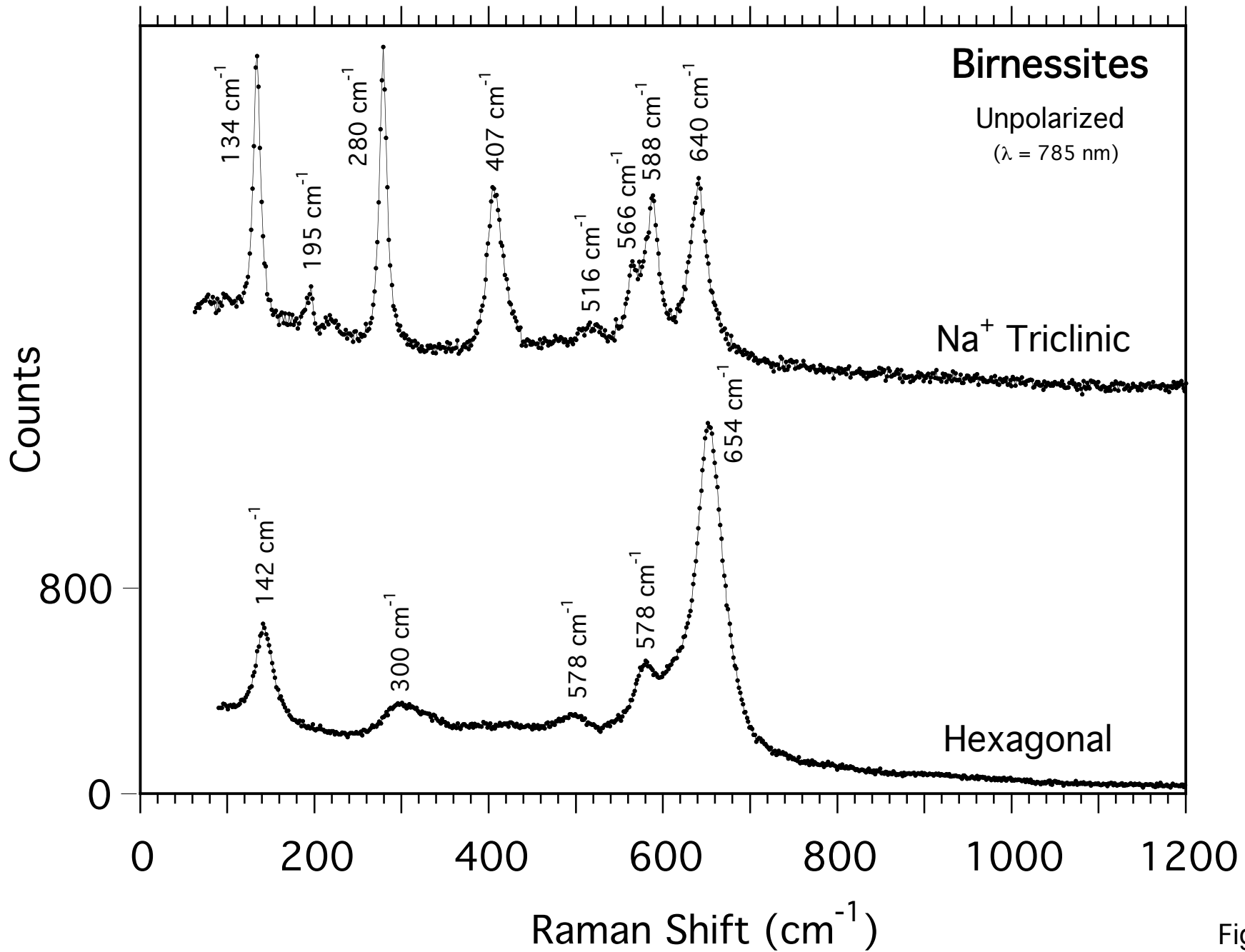


Fig. 11b

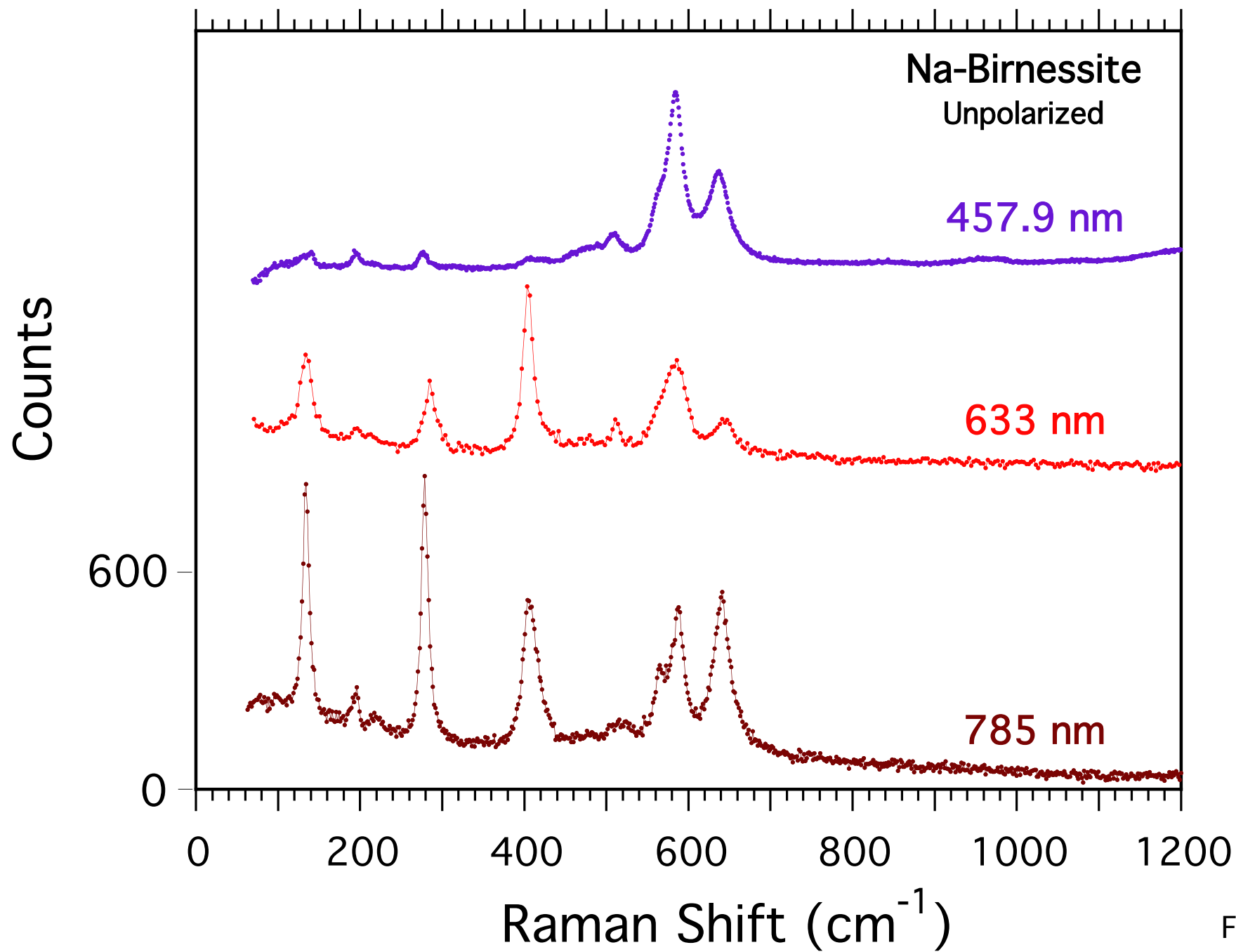


Fig. 12a

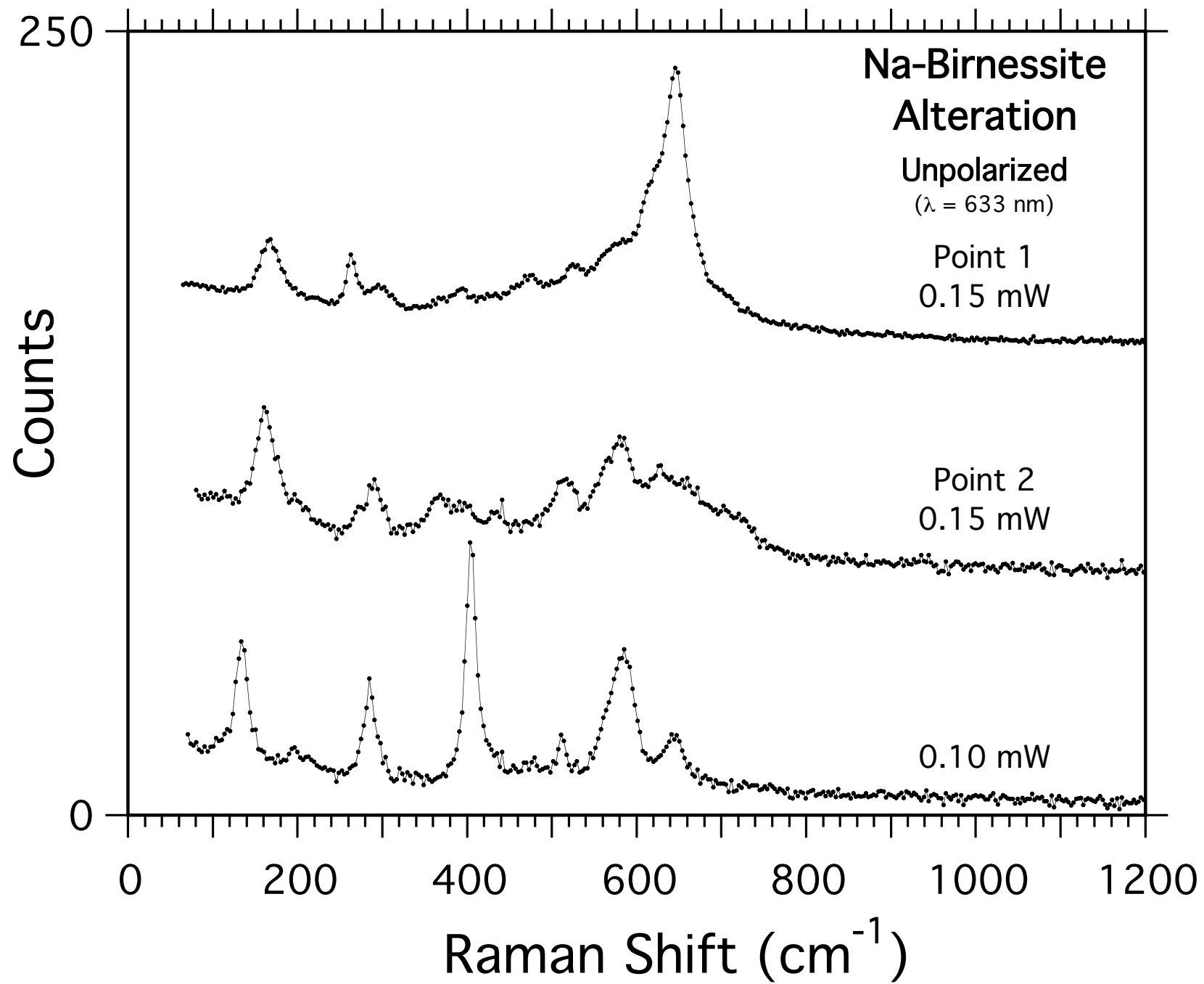


Fig. 12b

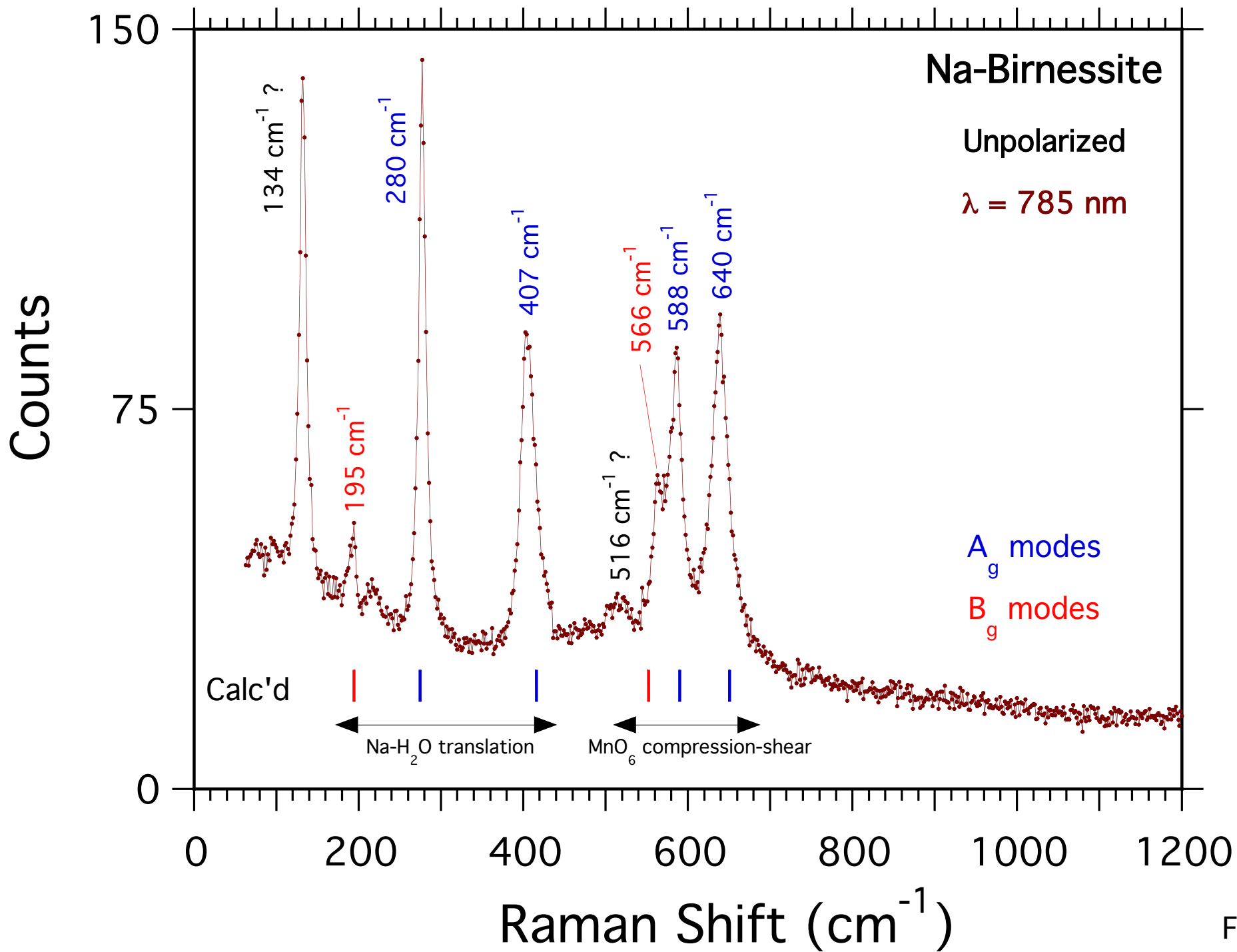


Fig. 13

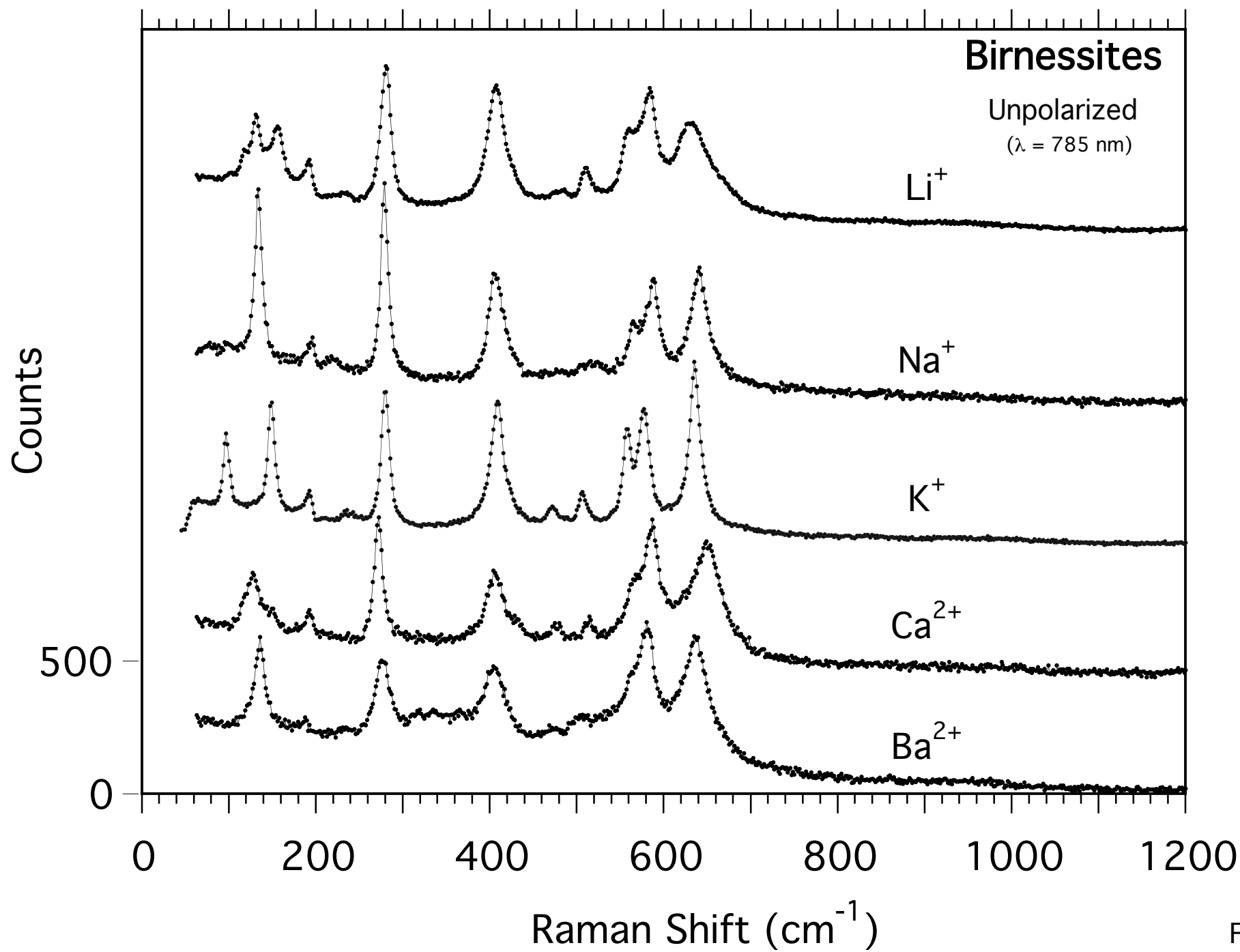


Fig. 14

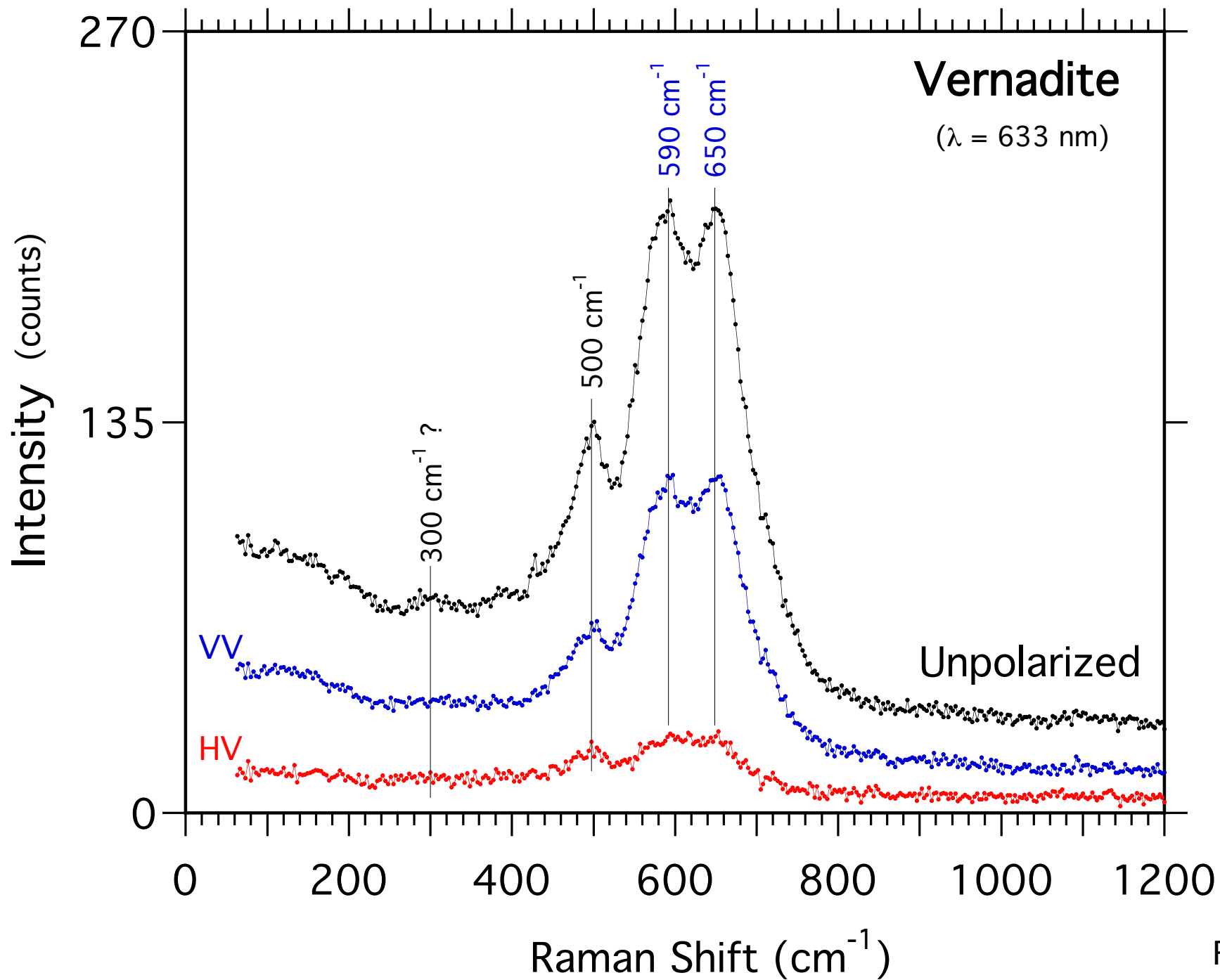


Fig. 15

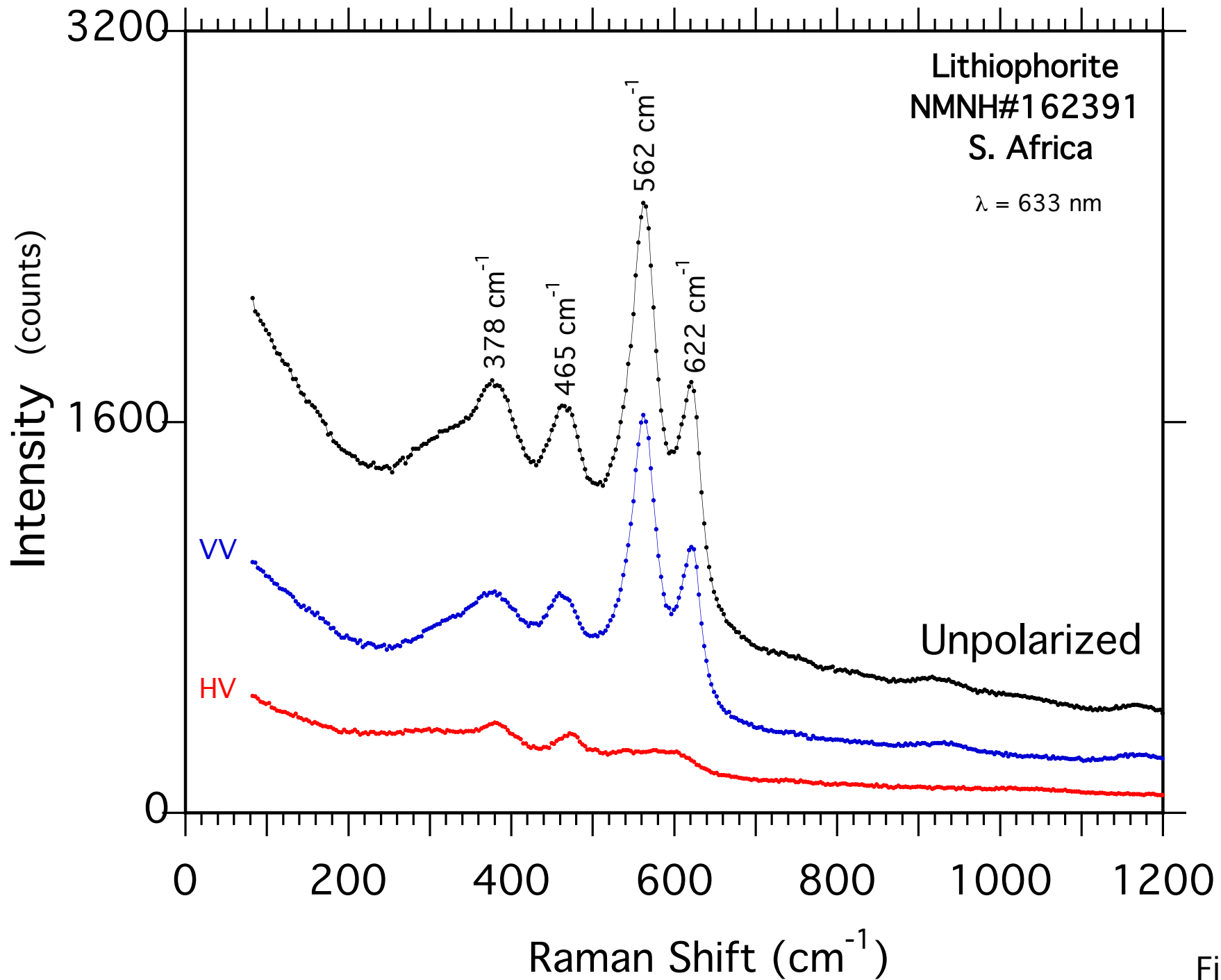


Fig. 16

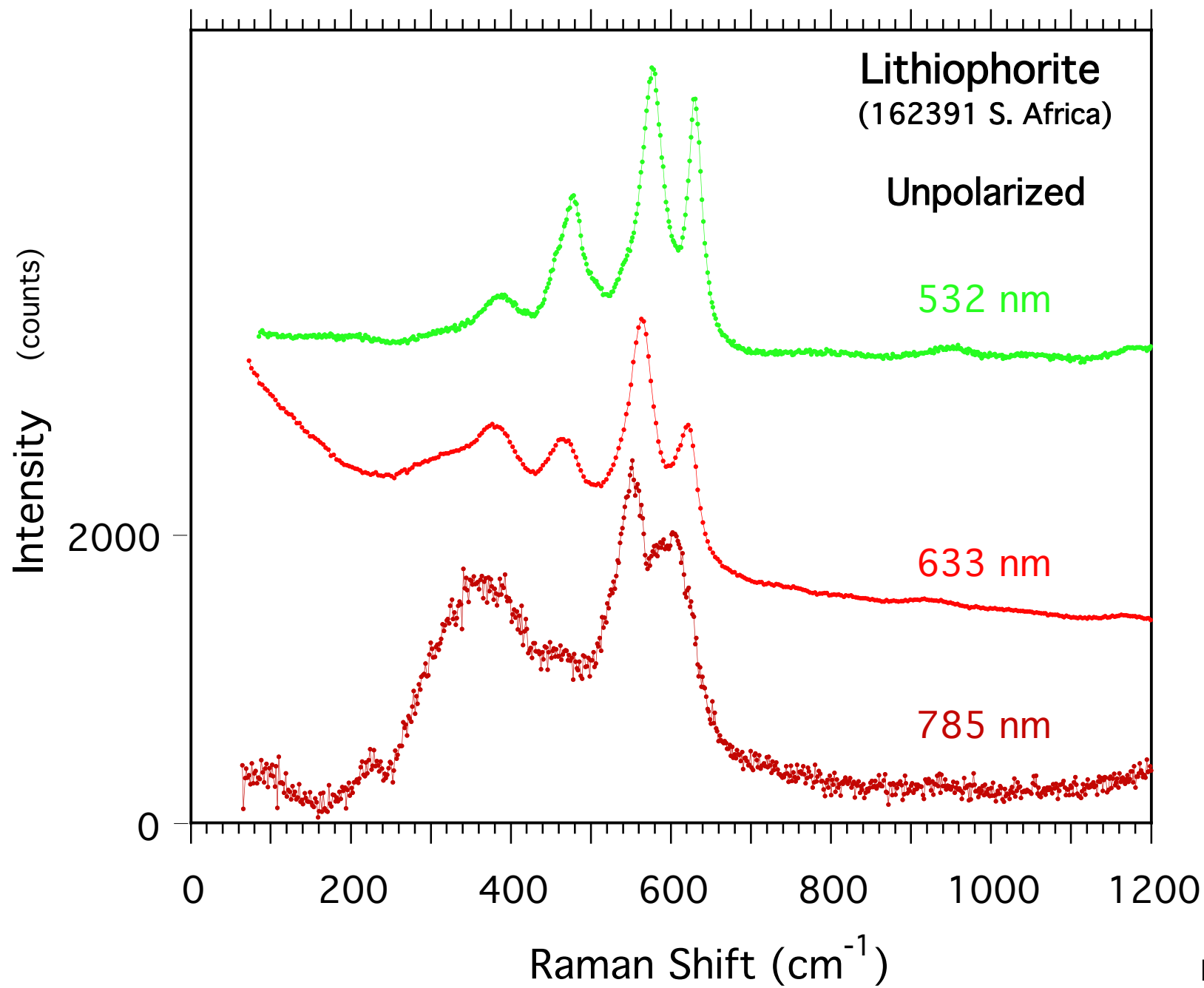


Fig. 17

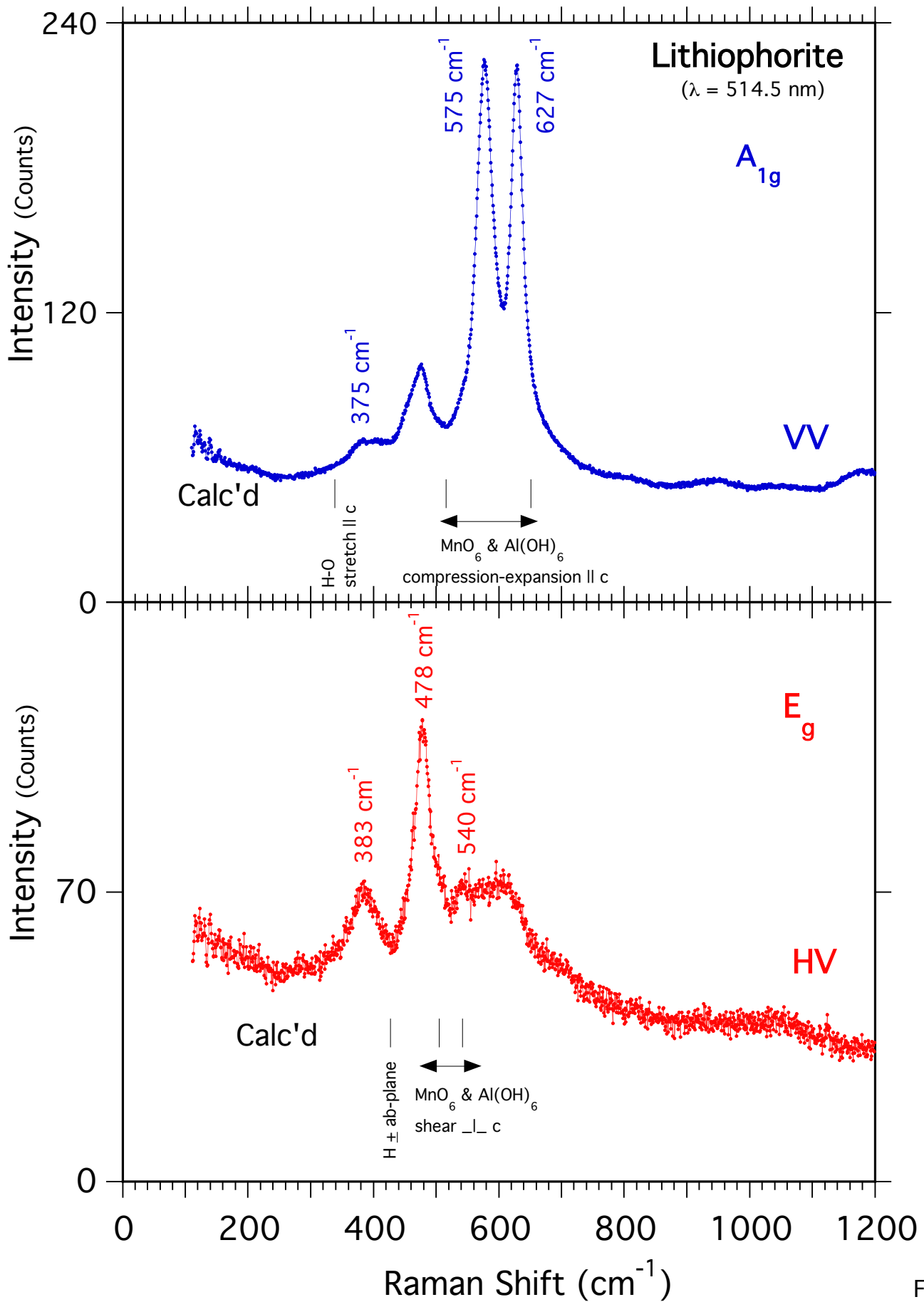


Fig. 18

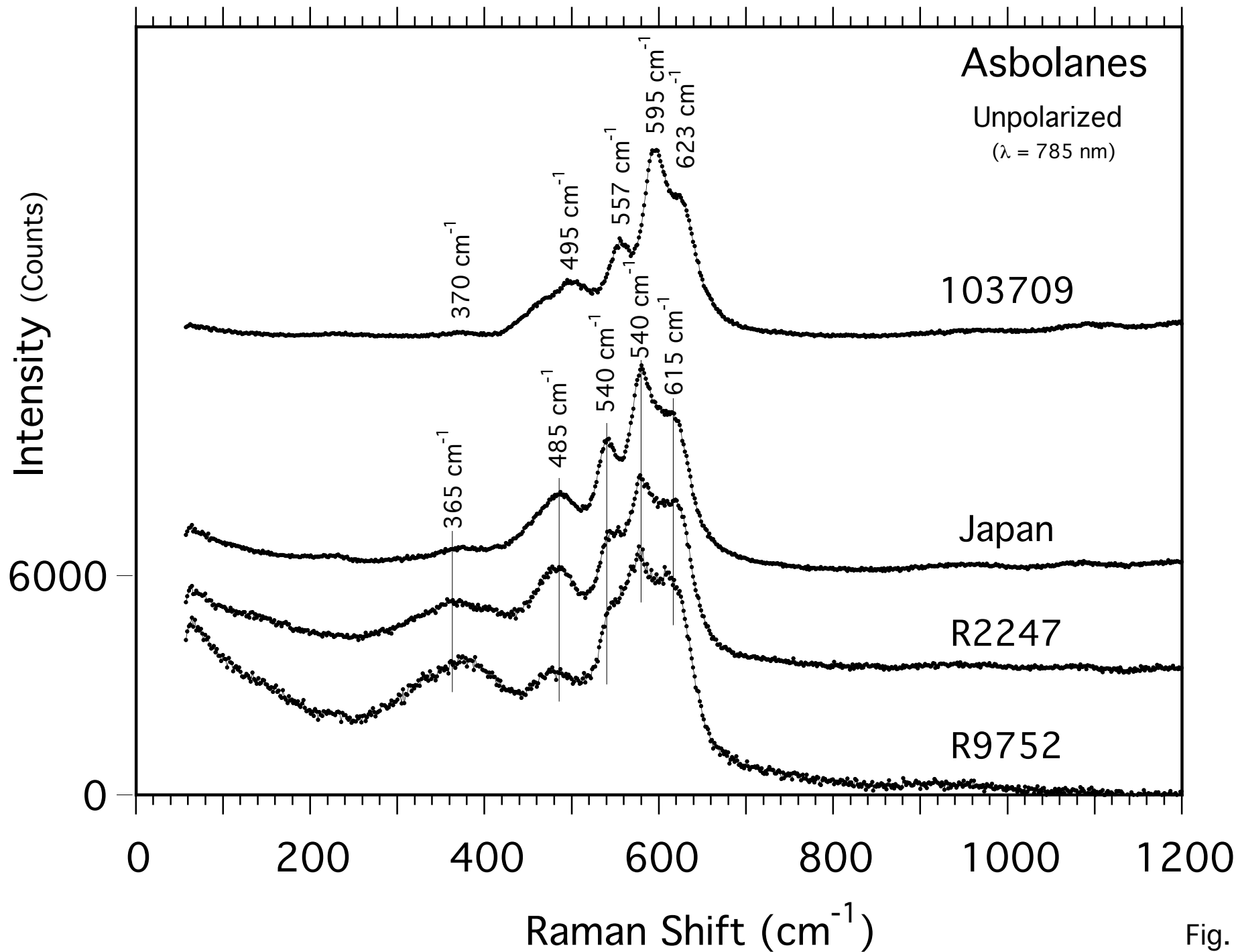


Fig. 19

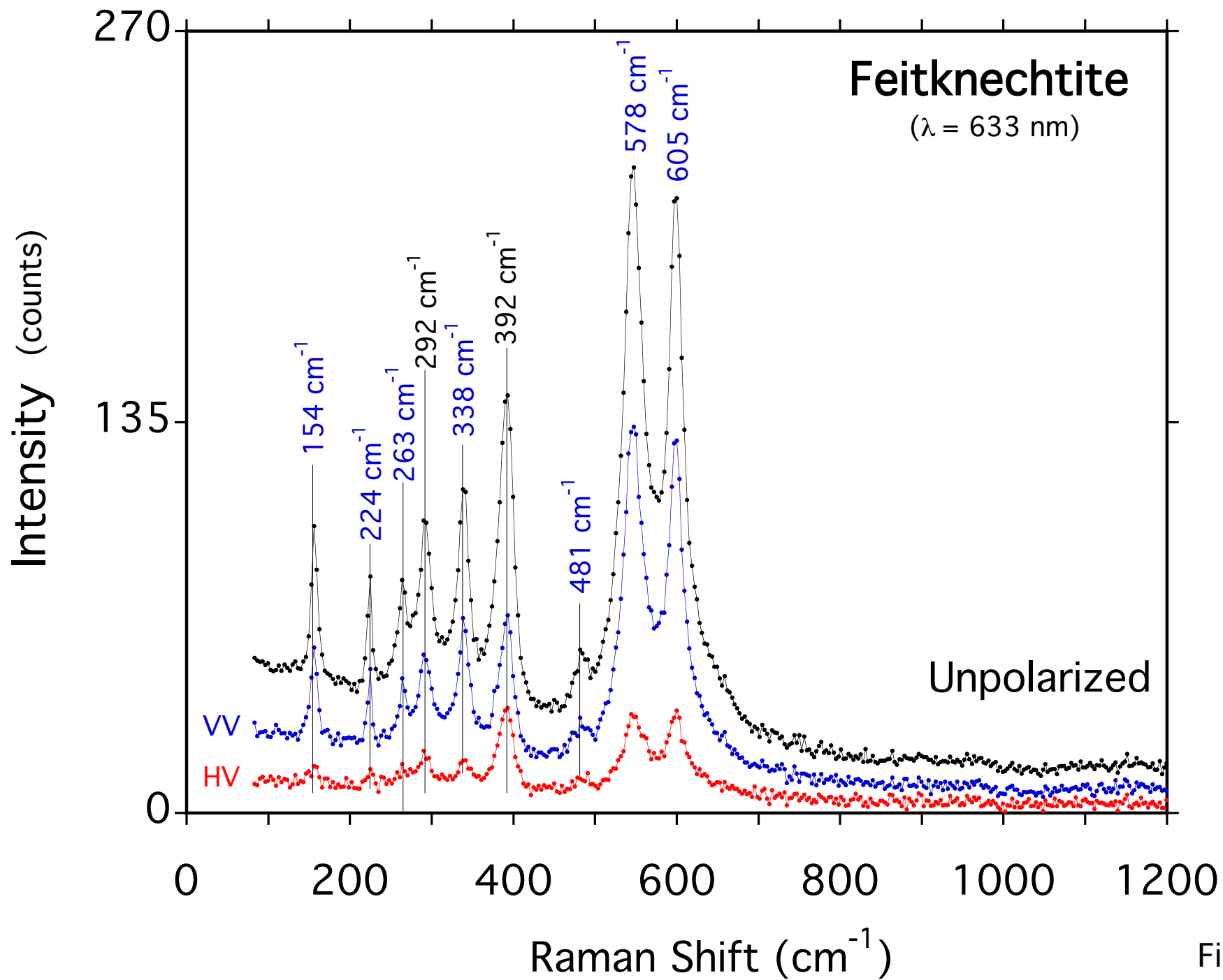


Fig. 20

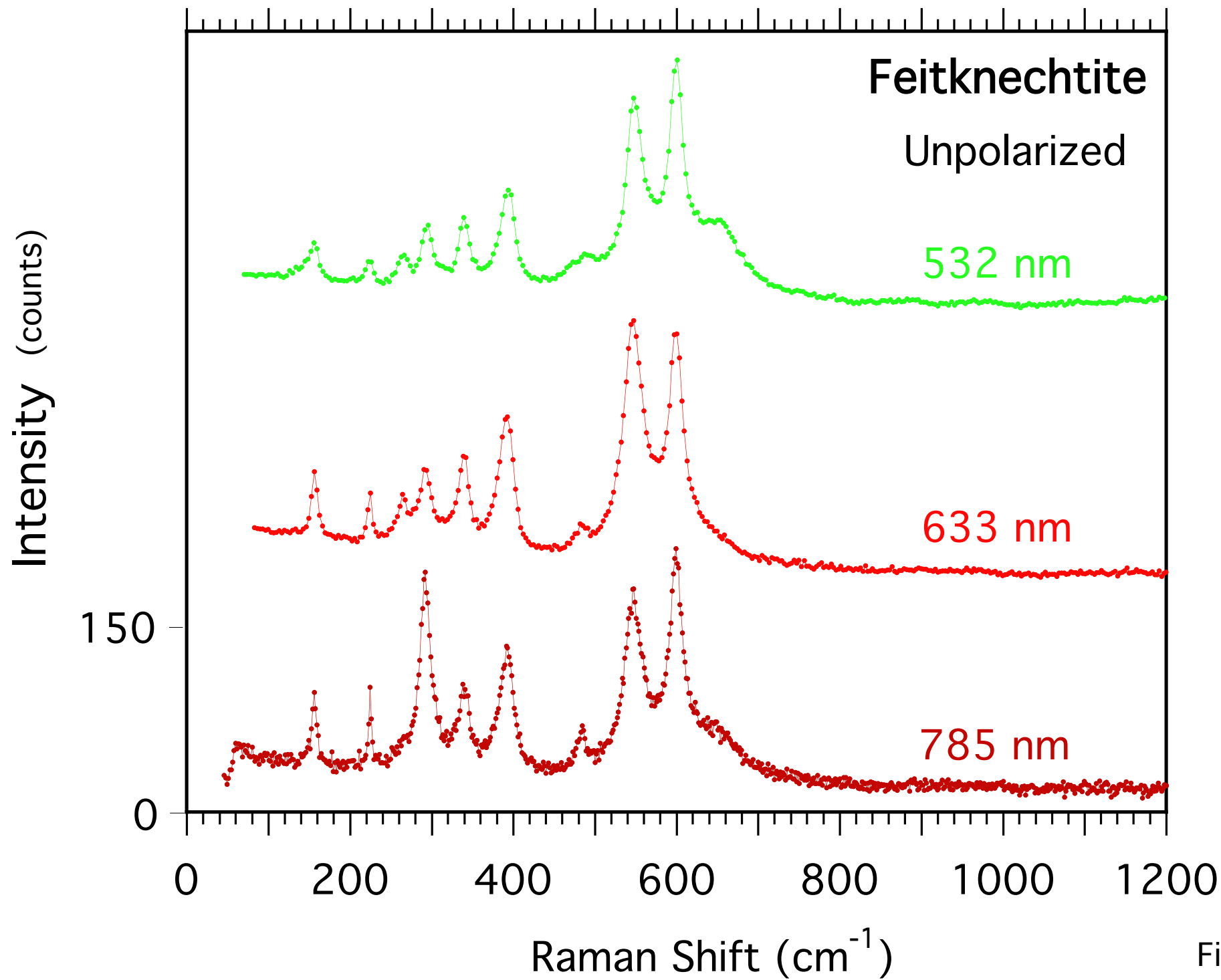


Fig. 21

Phylломanganates

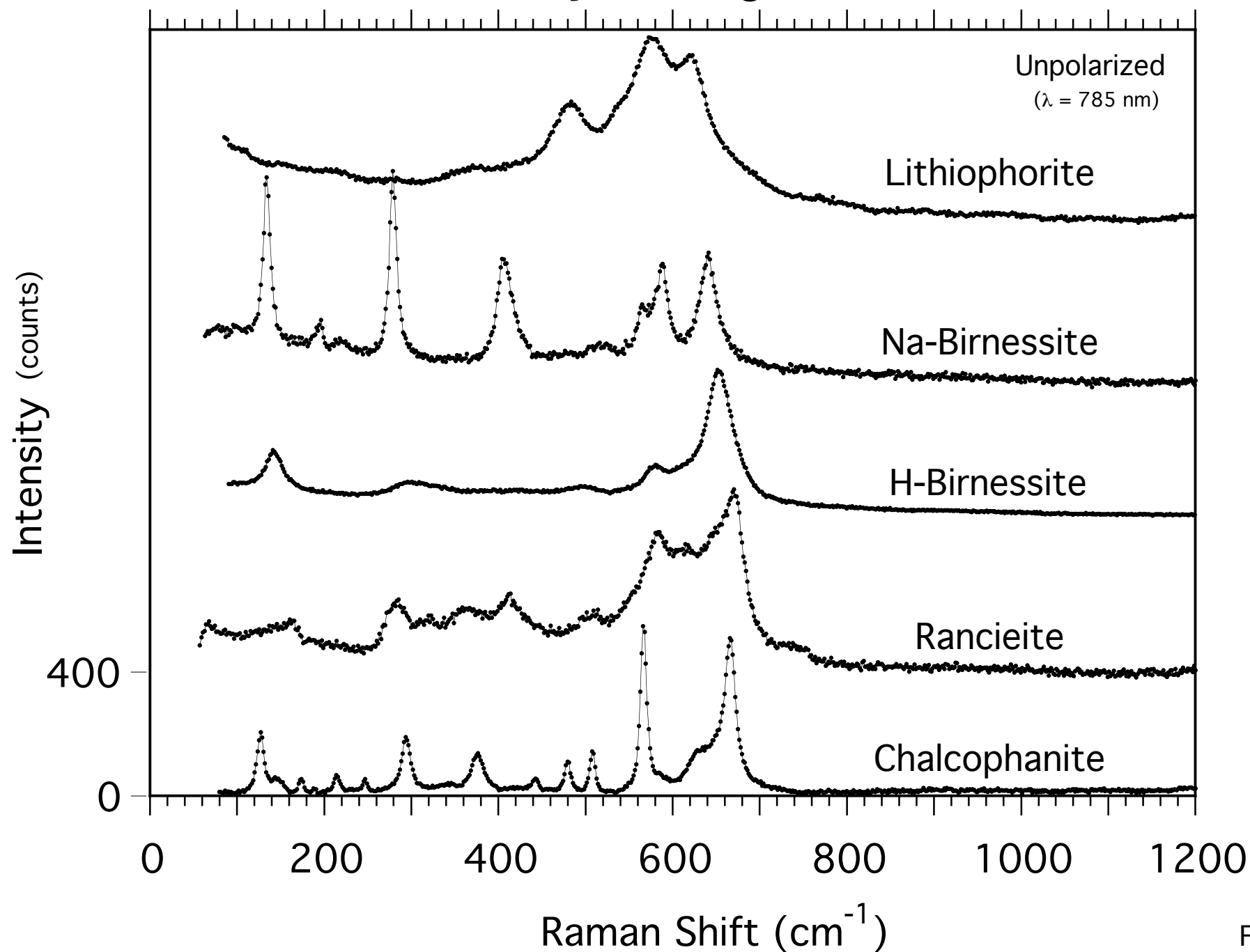


Fig. 22

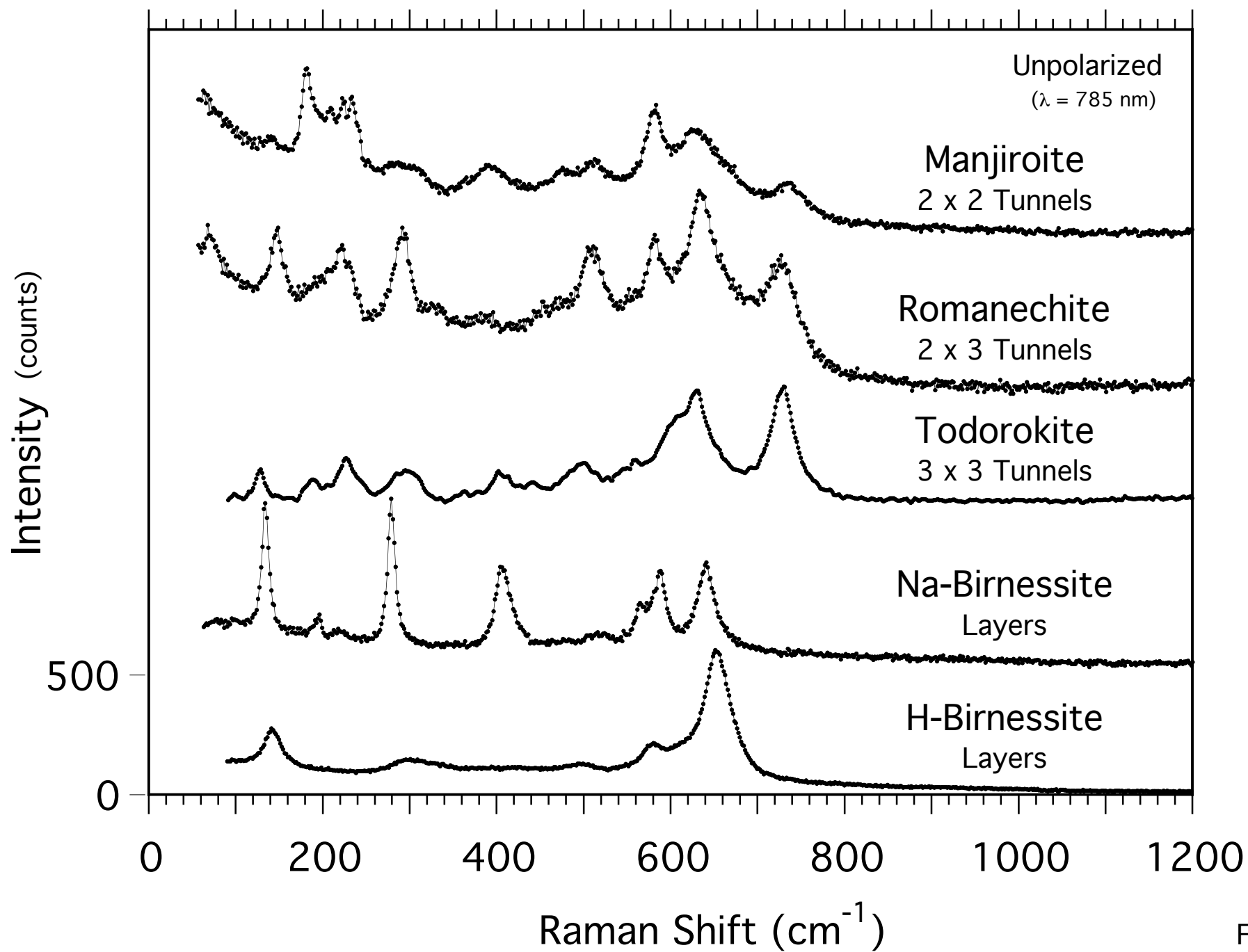


Fig. 23

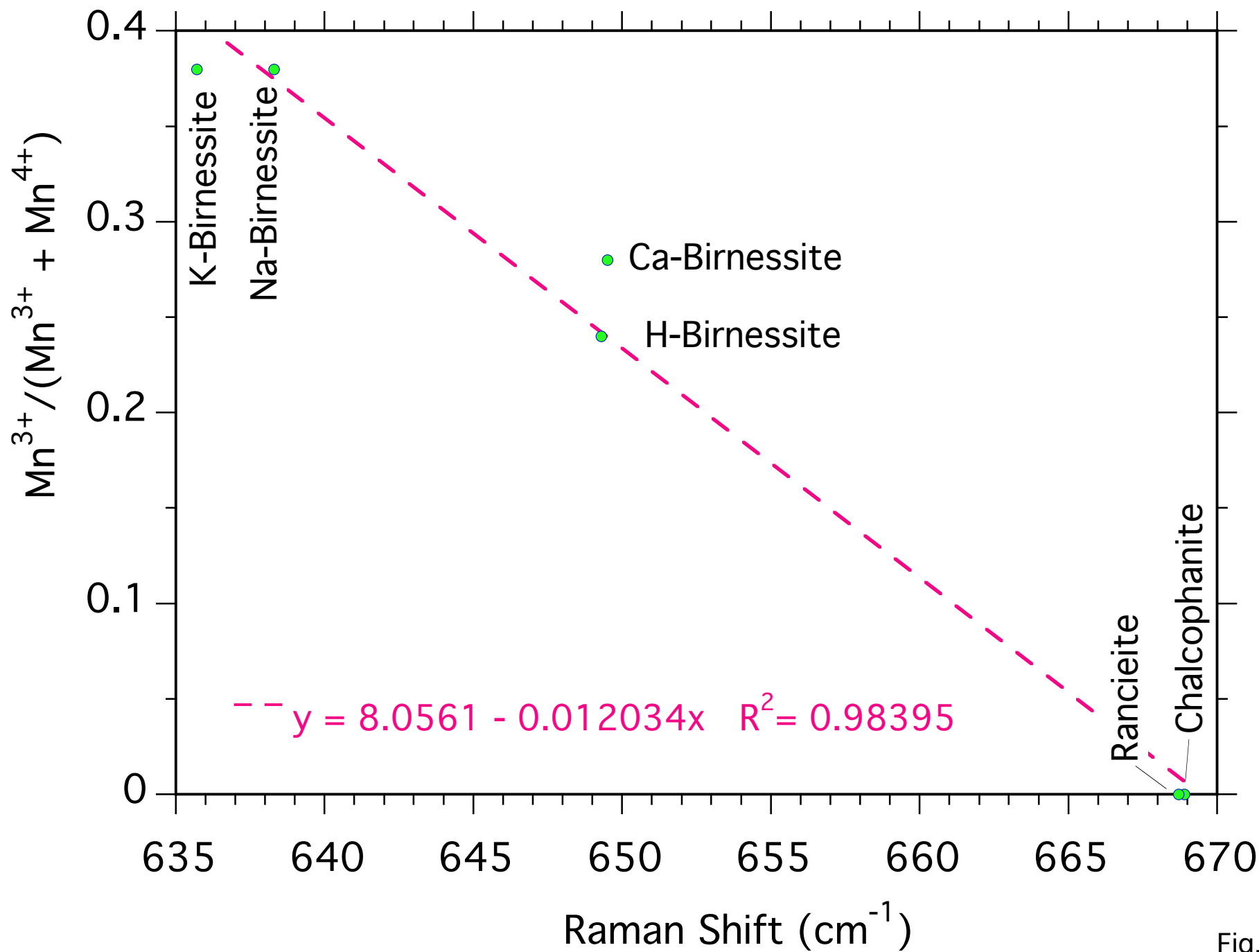


Fig. 24

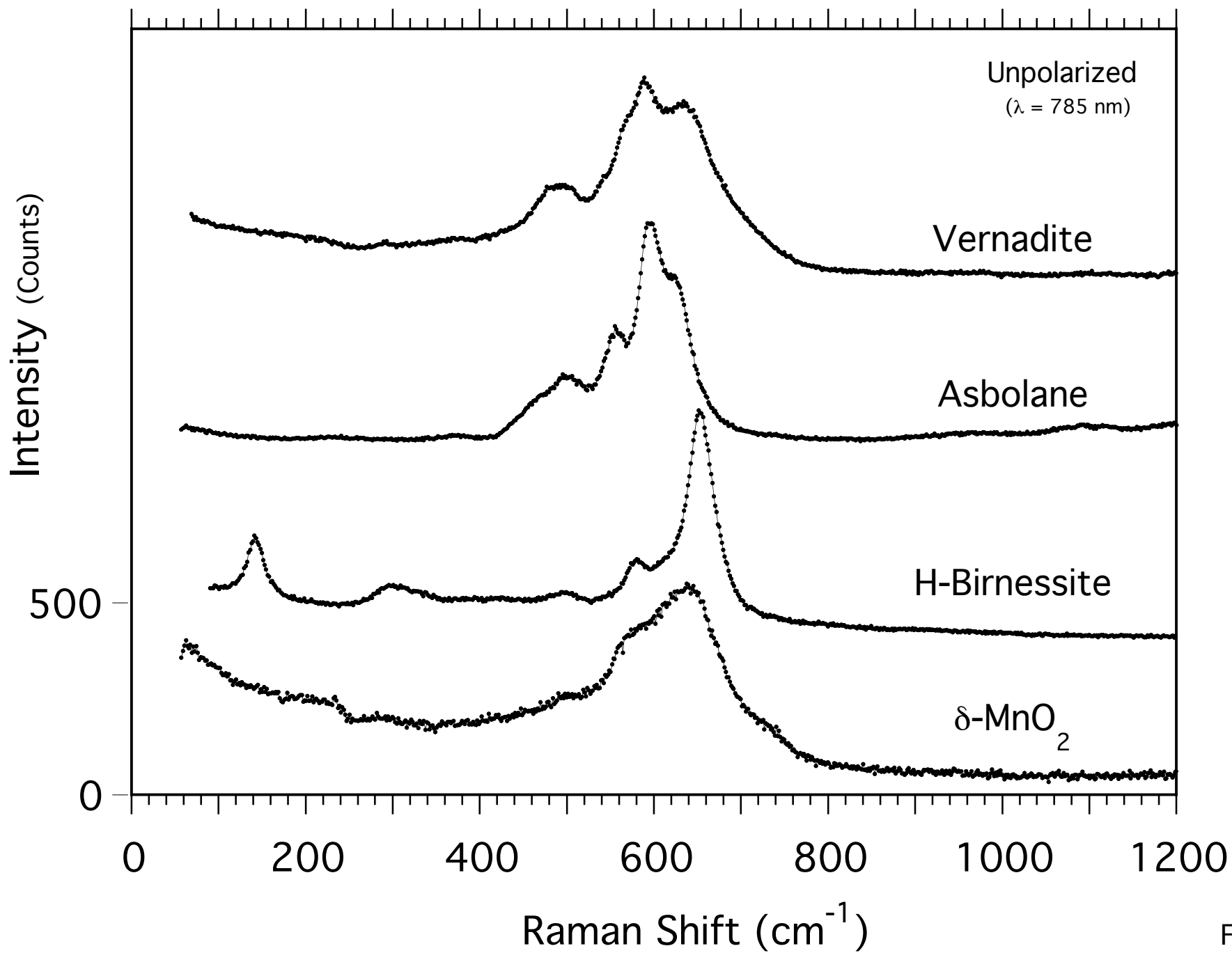


Fig. 25